Scientific Papers of
the Institute of Electrical Power Engineering of
the Wrocław University of Technology

PRESENT PROBLEMS OF POWER SYSTEM CONTROL

2

Oficyna Wydawnicza Politechniki Wrocławskiej
Wrocław 2012

Printed in the camera ready form

Institute of Electrical Power Engineering
Wrocław University of Technology
Wybrzeże Wyspiańskiego 27, 50-370 Wrocław, Poland
phone: +48 71 320 26 55, fax: +48 71 320 26 56
www: http://www.ie.pwr.wroc.pl/; e-mail: Inst.Energ@pwr.wroc.pl

OFICYNA WYDAWNICZA POLITECHNIKI WROCŁAWSKIEJ
Wybrzeże Wyspiańskiego 27, 50-370 Wrocław
http://www.oficyna.pwr.wroc.pl
e-mail: oficwyd@pwr.wroc.pl
zamawianie.ksiazek@pwr.wroc.pl

ISBN 978-83-7493-697-2

Drukarnia Oficyny Wydawniczej Politechniki Wrocławskiej. Order No. 789/2012.

CONTENTS

protective relaying,
stator differential protection,
split-phase protection

Sungsoo KIM*, Dale FINNEY**, Normann FISCHER**,
Bogdan KASZTENNY**

GENERATOR SPLIT-PHASE PROTECTION

The stator winding of a hydrogenerator is often made up of coils with multiple turns in the same slot. It is therefore possible for faults to develop between adjacent turns on the same phase (turn-to-turn faults). These faults cannot be detected by the stator differential protection because there is no difference between the neutral- and terminal-side currents. Split-phase protection, an overcurrent element responding to the difference between the currents in the winding parallel branches, is typically provided to detect these faults. Ideally, the split-phase element should be sensitive enough to detect a single shorted turn. Despite the fact that the current in this turn can be six to seven times the machine nominal current, the current seen by the split-phase protection can be quite small, in the order of one-twentieth of the generator full-load current. In addition, a spurious split-phase current can be measured due to current transformer (CT) errors, saturation during external faults in particular. Therefore, primary considerations in the application of split-phase protection are the method of measuring the difference in the currents between the parallel branches and the proper selection of the CT used for this purpose.

1. INTRODUCTION

We begin this paper with a review of stator winding construction, which provides an insight into how a turn-to-turn fault develops and how it is manifested as a circulating current. Next, we examine present practices used in split-phase protection and their relative performance in terms of sensitivity, security, and speed. This leads to a discussion of current transformers (CTs) as a source of split-phase current. Operating experience, settings guidelines, and CT selection criteria are covered next. The paper concludes with novel methods to improve the sensitivity, speed, and security of the split-phase element.

* Ontario Power Generation,
** Schweitzer Engineering Laboratories, Inc.,

2. HYDROGENERATOR STATOR DESIGN

2.1. UNDERSTANDING CONSTRUCTION OF STATOR WINDINGS

Rated frequency is proportional to the number of poles and rotational speed of the generator. Generators with hydraulic turbines as prime movers are constructed with a larger number of poles because they operate with a relatively slower rotational speed. The number of stator slots in a hydrogenerator is, in turn, closely related to the number of poles of the machine. Furthermore, the number of winding parallel branches is determined by the number of stator slots [7]:

$$n_p = \frac{N_S T_C}{3T_{PH}} \tag{1}$$

where:

N_S is the number of stator slots,

T_C is the number of turns per coil (winding dependent),

T_{PH} is the number of turns per phase.

As a result, the low rotation speeds of hydraulic turbines encourage the designing of generators with parallel branch stator windings (n_P is proportional to N_S). The designers can manage the number of parallel branches with the number of turns per phase (n_P is inversely proportional to T_{PH}).

The turns per phase (T_{PH}) are determined early in the machine design based on the following relationship:

$$T_{PH} = \frac{k_1 k_2 V_{PH}}{4.44 f \varphi} \tag{2}$$

where:

k_1 is the pitch factor of the stator winding (>1.0),

k_2 is the spread factor of the stator winding (>1.0; for most designs, $k_1 \cdot k_2 \simeq 1.1$),

V_{PH} is the rated phase-to-neutral voltage,

f is the nominal frequency,

φ is the flux (typical maximum flux density [B_M] in hydromachines is in the order of 0.6 to 0.7 T).

The number of the turns per coil (T_C) depends on the type of winding selected (n_P is proportional to T_C). Typically, a bar winding may only have one turn, whereas a coil winding consists of two or more turns.

Many factors influence the type of winding to be used, but in general, multiturn coil windings are used because they are more cost-efficient to manufacture (multiturn coils are wound by machine). The coils are wound such that adjacent turns have the smallest possible voltage difference between them. This allows the interturn insulation thickness to be minimized.

In the past, most large hydrogenerators in Europe and the United States used multiturn lap-connected coils. Machine designs originating in Russia used a single-turn, bar winding, wave-connected design. In large machines, it becomes difficult to insert each coil leg of a multiturn coil simultaneously into different slots. Roebel bar windings are manufactured in half-turn segments, making installation much easier on large machines. These single-turn designs have other advantages, as we will see later in this paper. Today, multiturn coils can be found on hydromachines with ratings of up to 150 MVA and 18 kV, with Roebel bar windings used for larger machines [8].

Once the number of stator slots, the type of winding, and the connection method have been determined in a given machine design, the distribution of the conductors in a given phase around the periphery of the stator must be decided. Typically, the designers can decide between a single-layer winding with varying coil pitch or a double-layer winding with varying coil pitch. The two types of windings with different pitch for a 24-slot machine are shown in Fig. 1.

The material used to insulate the winding is dependent on the type of coils composing the winding and varies by manufacturer. Single-turn bars are typically wrapped with asbestos or glass insulated strand tape. The insulation for multiturn coil windings is composed of two parts: epoxy novalak mica paper tape for the slot portion and isopthalate varnished mica flake tape for the end winding.

Figure 2 shows the conductor arrangement for two different windings. The slot width in a hydromachine will rarely exceed 1 inch (2.5 centimeters) while Fig. 3 shows slots of a typical hydrogenerator.

When examining Fig. 2a and considering the typical insulation used for this design, we notice that the two single bar winding coils are insulated from one another by a bakelite separator and an asbestos or glass stranded tape.

When examining Fig. 2b and considering the typical insulation used for this design, we notice that the separation between the two-turn coil windings is only bitumen mica tape. Through-fault conditions and variation in load result in the winding coils moving with respect to one another. This relative movement creates friction, which wears away the insulation between the windings over time. For the single-turn bar design, the friction is not an issue because the two single-turn bar windings are separated not only by their winding insulation material but also by a tough bakelite insulation material. The two-turn coil winding does not have this advantage, and over time, this movement between coils will result in a turn-to-turn fault.

Voltage surges present another failure mechanism. At power system frequencies, the voltage is distributed linearly throughout the winding. However, this desired desired situation is not the case during a fast front voltage surge where a much greater percentage of the surge appears across the first few turns.

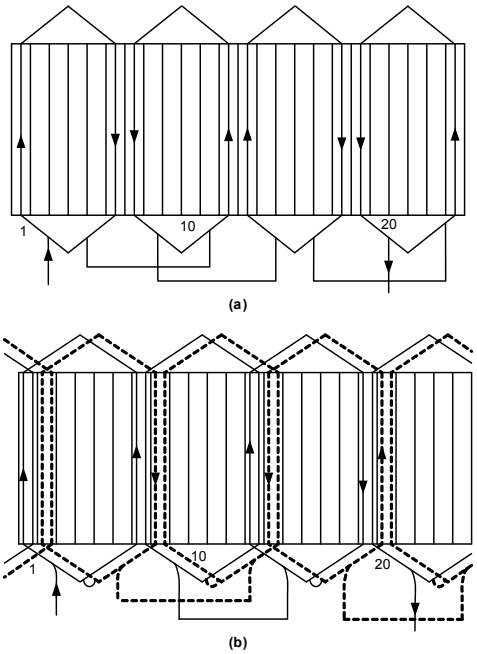

Fig. 1. Single-layer wave winding with a pitch of 0.83 (a), double-layer wave winding with a pitch of 1 (b)

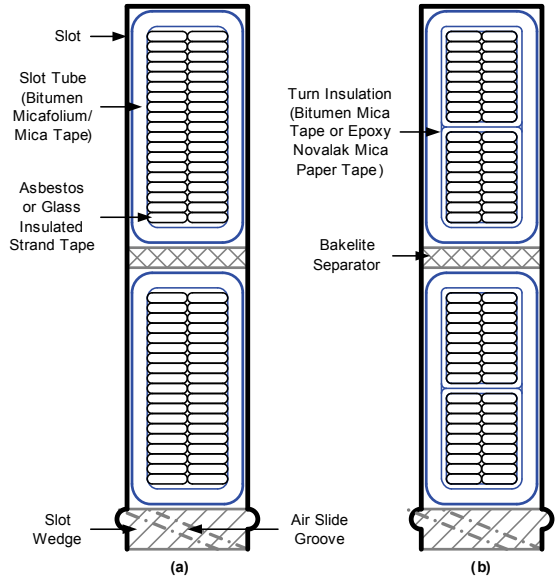

Fig. 2. Single-turn bar winding configuration (a), two-turn coil winding configuration (b)

Fig. 3. Single-turn bar winding configuration (a),
Two-turn coil winding configuration (b)

An important point should be evident in the preceding discussion: when single-turn bar windings are used in a hydrogenerator, turn-to-turn faults are not a concern. For other designs, however, turn-to-turn faults must be considered as realistic failure modes of the protected machine.

2.2. CURRENT DUE TO TURN-TO-TURN FAULTS

Now, we examine the impact of turn-to-turn faults. Consider a winding with two parallel branches, and assume that there is one turn on one of the A-phase branches shorted, as shown in Fig. 4.

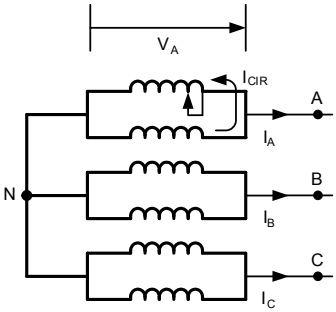

Fig. 4. Turn-to-turn fault in a two-winding machine

If we examine the A-phase winding, we realize that the differences between the two windings result in a circulating current. The current that circulates because of a shorted turn is primarily dependent on two factors.

First, the shorted turn reduces the voltage in the branch by an amount proportional to the line-to-neutral voltage divided by the total number of turns in the branch. This voltage difference drives a current, which circulates through the parallel branches. The net magnetomotive force adds to zero around the circuit, and consequently, the associated flux does not cross the air gap. This current is therefore limited only by the leakage reactance.

Second, an added flux is produced by the current flowing in the shorted turn. If we assume rated current is flowing at the generator and think about the shorted winding behavior as an autotransformer, then the current in the shorted turn can be estimated as the product of the nominal current and the total number of turns making up the circuit (ampere-turn balance). This large current couples strongly with another coil in the same slot. Depending on the configuration of the winding, this coil may be part of the same phase or a different phase. If it is a part of the same phase, then the induced current acts to reduce the current produced by the voltage difference (the first factor mentioned previously).

Figure 5 shows a simplified equivalent circuit for calculating the circulating current based on the previous observations. Not surprisingly, this circuit resembles the case of two transformers in parallel but on different taps.

The equivalent circuit contains the driving force and the limiting impedance, allowing us to approximate the circulating currents as follows:

$$I_{CIR} = \frac{k\dfrac{V_A}{n}}{X_{Laa1} + X_{Laa2'}} \tag{3}$$

where:

$\dfrac{V_A}{n}$ is the voltage per turn,

n is the number of turns,

k is the number of shorted turns,

X_{Laa1} is the leakage reactance of Branch 1,

$X_{Laa2'}$ is the leakage reactance of Branch 2.

For windings with two parallel branches, the leakage reactance for the unfaulted branch (X_{Laa1}) will be twice the value provided in the machine data sheet. However, determining the leakage reactance of the faulted winding ($X_{Laa2'}$) may be difficult, as explained previously.

While it is adequate to consider Fig. 5 and the associated (3) for the understanding of the circulating current, there are difficulties in applying the equation in practical situations and limits to its accuracy. The *IEEE Tutorial on the Protection of Synchronous Generators* [3] lists a typical value for the circulating current due to a shorted turn of 4 percent of the generator full-load current. Whenever possible, the generator manufacturer should be consulted for an accurate value.

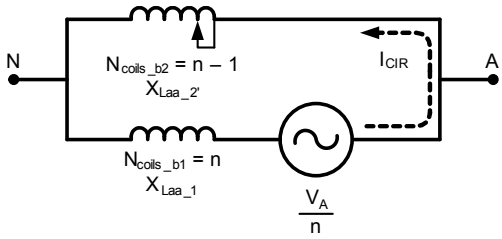

Fig. 5. Simplified equivalent circuit for a turn-to-turn fault in a machine

2.3. CURRENT DUE TO TURN-TO-TURN FAULTS

Figure 6 is a vector diagram illustrating the difference between the winding currents for a turn-to-turn fault. Analyzing the vector diagram, we can conclude that detecting a turn-to-turn fault should not be too complex because there is a difference between the currents in both magnitude and angle. This implies that a protection scheme operating on the difference between the branch (*W*1 and *W*2) currents is well-suited for detecting these types of faults.

An important observation that can be made from Fig. 6 is that the difference current (I_{DIF}) during a turn-to-turn fault is dependent on the circulating current and the load current.

The circulating current (I_{CIR}) is determined by the number of turns that are short-circuited and the volts-per-turn value of the machine. Because neither of these two factors changes during a turn-to-turn fault, the circulating current does not depend on the machine load.

The load current (I_{LOAD}) is dependent on two factors:

- The active power load connected to the machine.
- The percentage excitation (or in other terms, the power factor) of the machine.

Both these factors change during the normal operation of the machine, which implies that the differential current varies as the power factor and active power supplied by the machine vary.

It is easy to understand why the load current varies proportionally with the variation of the active load, but understanding why the excitation of the machine affects the load current is less intuitive. To explain this, we consider the equation for the voltage at the A-phase terminals of the machine:

$$V_{A\_TERM} = -r_S I_A - \frac{d\lambda_A}{dt} \tag{4}$$

where $d\lambda_A$ is a flux linkage of the A-phase.

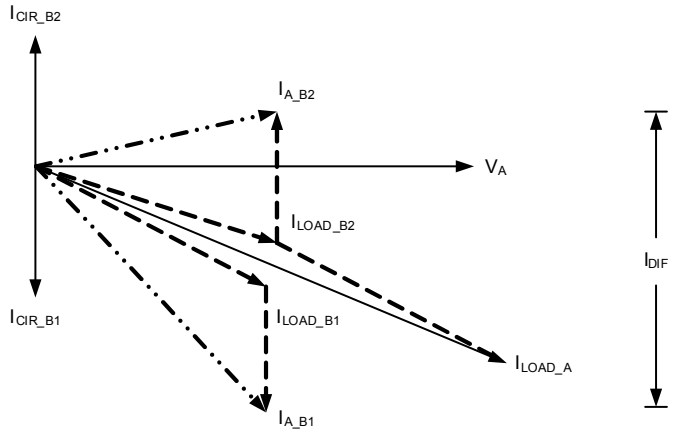

Fig. 6. Phase diagram showing the relationship between the terminal voltage, load current, and circulating current for a turn-to-turn fault in a machine

Typically for a machine, the resistance of the stator winding (r_s) is much lower than the inductance of the winding, and as such, we can ignore it for all practical purposes. Therefore, the terminal voltage of the machine can be approximated by a simplified equation:

$$V_{A\_TERM} = -\frac{d\lambda_A}{dt} \tag{5}$$

The terminal voltage of the machine is held constant by the voltage of the power system. This implies that the flux linkage of the machine is constant. The flux linkage of the machine is determined by the following:

$$\lambda_A = L_{AA} I_A + L_{AB} I_B + L_{AC} I_C + L_{AF} I_{F\_DC} \tag{6}$$

where:

L_{AA} is the self-inductance of the A-phase winding,

L_{AB} is the mutual inductance between the A- and B-phase windings,

L_{AC} is the mutual inductance between the A- and C-phase windings,

L_{AF} is the mutual inductance between the A-phase and field windings.

The first three terms of (6) are responsible for what is known as armature reaction. Assume that the machine is connected to a power system and is not exporting any real power and the field current (I_{F_DC}) is such that it fully supports the flux linkage of the machine required to maintain the terminal voltage of the machine. This means that the phase currents (I_A, I_B, and I_C) are zero. If we now wish to export reactive power (VARs) from the machine, we simply increase the field current, thereby increasing the flux linkage between the field and A-phase windings. Because the total A-phase flux linkage has to remain constant, the flux linkage created by the mutual coupling and

self-coupling of the armature windings has to be such that it opposes the increase of flux linkage created by the field winding. In other words, changes in the field current required to change the reactive power result in changes in the stator current and, consequently, in the differential current.

Similarly, if we wish to import reactive power, we decrease the field current, thereby decreasing the flux linkage between the field and A-phase windings, resulting in the flux linkage of the mutual windings and self-windings having to enforce the flux linkage of the field winding.

Figure 7 illustrates the three scenarios described above. Now that we understand how both power and power factor affect the load current of the machine, we see how they influence the abilities of a device that measures the difference current between two branches on the same winding. Figure 8shows the differential current for a machine with a turn-to-turn fault under lightly loaded conditions (Fig. 8a) and heavily loaded conditions (Fig. 8b).

From Fig. 8, we can see that when the machine is lightly loaded, the differential current is pronounced because it is mostly related to the constant circulating current. However, when the machine is heavily loaded, the load current tends to mask, or bury, the circulating current, resulting in the less pronounced differential current.

Other phenomena that produce natural variations in the circulating current are reviewed in Section V.

In all discussions so far, we have assumed that the winding branches are identical and that they have the same inductance. In practice, however, this is not the case because of manufacturing tolerances, such as differences in the construction of each of the branches and variations in the air gap. These differences between the parallel branches result in a natural (standing) circulating current occurring between the branches without any turn-to-turn faults. These differences also result in a transient circulating current during external fault conditions, as explained in Section IX.

2.4. OPERATION OF HYDROGENERATORS WITH BYPASSED COILS

Should a stator fault develop in a hydrogenerator, the protection system will trip the machine offline. It may be desirable to put the machine quickly back into service. Therefore, a temporary repair can be performed. This typically involves cutting out and bypassing the faulted coil. The faulted coil is left open-circuited, and the machine is placed back into service.

The asymmetry introduced into the winding by this repair can have a significant impact on the machine operation. Unbalanced currents cause heating of the rotor. Unbalanced mechanical forces produce vibrations and can cause the rotor to rub the stator [1]. As a result, the loading on the machine will likely need to be reduced during bypassed coil operation. In some cases, healthy coils in other branches are also bypassed in order to make the stator more symmetrical and limit the level of unbalance. In addi-

tion, the bypassed coil can have a significant impact on the quiescent value of the circulating current (see Fig. 9).

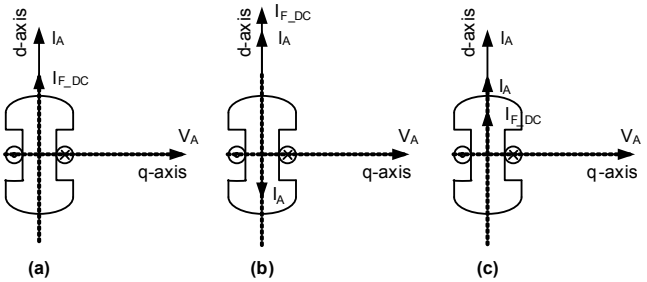

Fig. 7. Relationship between the field current, flux, terminal current, and terminal voltage for a nominally excited machine (a), underexcited machine (b), and overexcited machine (c)

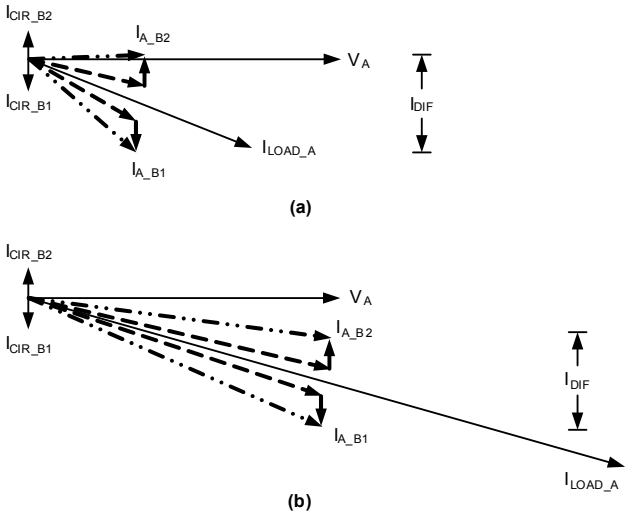

Fig. 8. Phasor diagram showing the relationship between the circulating current, load current, and difference current under lightly loaded conditions (a) and heavily loaded conditions (b)

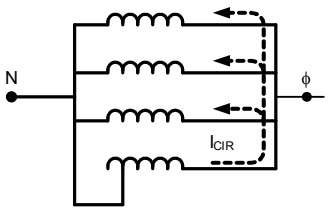

Fig. 9. Winding with a bypassed coil (one phase shown)

The magnitude of the current that circulates because of the bypassed coil differs depending on the winding configuration (alternate pole versus adjacent pole) and on the winding pitch [6]. There can also be a significant coupling with the other two phases of the winding [5]. As a result, the circulating current can be elevated in each phase to varying degrees.

The level of the circulating current can also exhibit a strong correlation with generator loading with a significant difference in the circulating current (up to 25 percent) observed between no-load and full-load conditions [2].

The increased value and variation in the circulating current impact the settings of the split-phase protection. Section V addresses this issue in more detail.

3. STATOR SHORT-CIRCUIT PROTECTION

Traditionally, each phase of a hydromachine stator winding is constructed of two, four, or eight parallel branches with each branch having several coils and each coil having a number of turns, as described in Section II. The significance of these design styles is two-fold:

- Turn-to-turn faults are possible in such configurations.
- An additional means of detecting stator faults is now possible by effectively comparing currents from the parallel branches–split-phase protection.

The stator winding may be protected by either a dedicated (independent) differential element and a split-phase protection element or a single protection scheme that is a combination of these two elements. Figure 10 illustrates how these schemes are typically applied.

If we examine the protection arrangement shown in Fig. 10a, differential protection (87G) is selected to protect the stator against phase faults but not against turn-to-turn faults. The stator phase-winding differential protection responds to the difference between the currents at the terminal and neutral sides of the stator phase (even if a phase is composed of multiple branches). During a turn-to-turn fault, the load current entering the phase with the faulted winding is still equal to the load current exiting the phase with the faulted winding. Therefore, 87G remains balanced and does not respond to the turn-to-turn fault. For detecting turn-to-turn faults, the machine is additionally equipped with a split-phase overcurrent-based protection element (Fig. 10a and Fig. 11).

An alternative solution is to devise a differential element that spans the entire winding and assumes the known split of the current between the parallel branches. Should this split be upset by the turn-to-turn fault and the resulting circulating current, the element responds. This approach (Fig. 10b) compares the branch current with an equal share of the total current, and as a result, it becomes unbalanced during a turn-to-turn fault, allowing detection of turn-to-turn and (at least in theory, subject to sensitivity limitations) phase and ground faults.

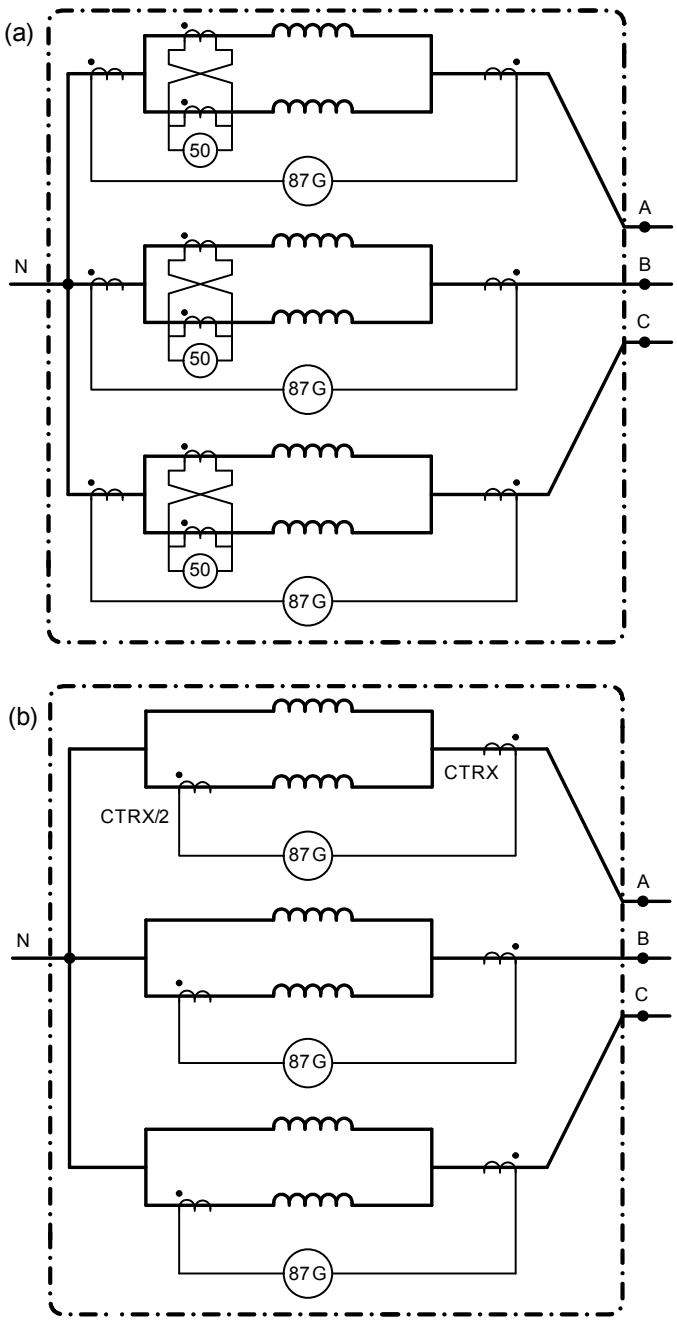

Fig. 10. Protection scheme with dedicated stator phase-winding differential and split-phase protection elements (a), a single protection scheme combining stator phase-winding differential and split-phase protection (b)

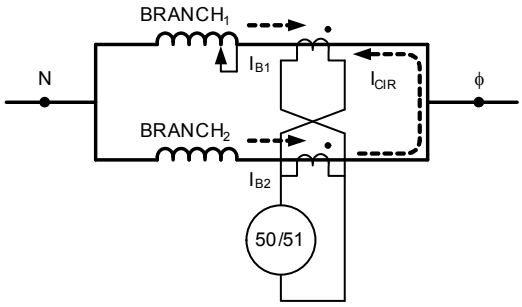

Fig. 11. Winding with a bypassed coil (one phase shown)

In the past, when generator protection was composed of discrete relays, the protection engineer might have had to choose between split-phase and differential protection. Invariably, split-phase protection was chosen because in addition to stator turn-to-turn faults, the split-phase scheme can detect stator phase and ground faults and even turn-to-turn faults in the rotor circuit [6]. Notably, several modern microprocessor-based relays provide either stator differential or split-phase protection, but not both.

3.1. SPLIT-PHASE OVERCURRENT PROTECTION

In the most commonly applied type of split-phase protection, the currents from the parallel branches are measured as two quantities, each representing approximately half of the total current, as shown in Fig. 11. The split-phase current, representing the difference between the two groups, is derived either from two differentially connected CTs or from a single- or dual-window, core-balance CT. The impacts of the choice of CT source are detailed in Section IV.

The split-phase current is applied to an overcurrent element. Both instantaneous and inverse-time elements may be applied. Because this method operates only from the split-phase current, it may be thought of as a low-impedance, differentially connected element. It has no inherent restraint mechanisms. Optimal setting of this element is the focus of Section V.

3.2. COMBINATION OF SPLIT-PHASE AND STATOR PHASE-WINDING DIFFERENTIAL ELEMENTS

In the combined split-phase and differential scheme shown in Fig. 10b, one CT (sometimes referred to as the split-phase CT) measures half of the total current and the other measures the total winding current. The ratio of the split-phase CT is half of the ratio of the phase CT. As a result, with no circulating current, the output of the two CTs adds to zero.

The currents from the two CTs are typically applied to a percentage differential element. This provides a restraint mechanism to secure the element under external faults and other conditions that lead to measurement errors.

However, we examine if this linear percentage differential element is sensitive enough to detect a turn-to-turn fault. The operating and restraint currents are determined as follows:

$$I_{OPERATE} = \left| I_{PHASE} + I_{WINDING} \right| \tag{7}$$

$$I_{RESTRAINT} = \frac{1}{2}\left(\left| I_{PHASE} \right| + \left| I_{WINDING} \right| \right) \tag{8}$$

We consider a machine with two parallel branches and capable of producing 4,000 A at full load. The split-phase CT is selected to be 2000/5. We assume a single turn-to-turn fault in this machine will produce a circulating current of approximately 80 A or 0.2 A secondary (4 percent of full-load current).

Using (7) and (8) and 5 A secondary as 1 pu, a differential protection element would derive the following operate and restraint currents:

$$\begin{aligned} I_{OPERATE} &= 0.04 \\ I_{RESTRAINT} &= 1.02 \end{aligned} \tag{9}$$

If we plot this on the percentage differential plane (Fig. 12), assuming a minimum pickup of 0.1 pu and a slope of 25 percent (typical for a generator relay), we can see that from a differential protection point of view, it plots solidly into the restraint region.

The example illustrates that the combined protection, based on a linear percentage differential element, would also fail to detect a single turn-to-turn fault. This scheme has a much lower sensitivity to turn-to-turn faults than the dedicated split-phase protection scheme does. What is more noteworthy about this scheme is that as the load current of the machine increases, the sensitivity of this scheme to detect turn-to-turn faults decreases.

Evidently, this scheme offers better security than other approaches (by using the restraint produced from both the load and external fault currents). However, we will see in Section IX that there are approaches to security that do not sacrifice sensitivity.

3.3. NEGATIVE-SEQUENCE DIFFERENTIAL

A lesser-known method that may be used for detecting turn-to-turn faults is the negative-sequence differential element. The protection scheme requires measuring the negative-sequence current entering and exiting the winding. The scheme can be realized as shown in Fig. 13.

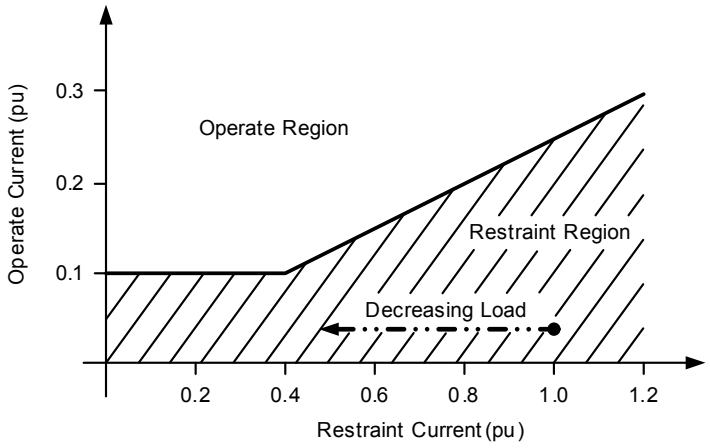

Fig. 12. Percentage differential characteristic with a turn-to-turn fault in the blocking region

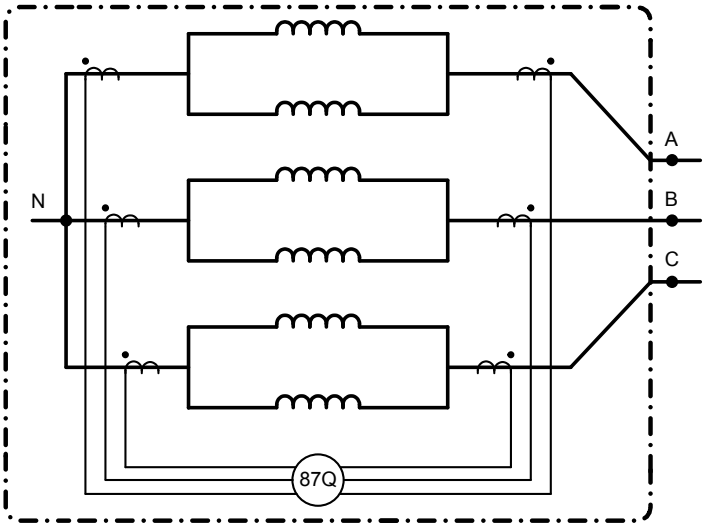

Fig. 13. Negative-sequence protection scheme that can be applied to detect turn-to-turn faults

This scheme can provide good sensitivity in detecting a turn-to-turn fault, but it has to overcome the same issues as the split-phase protection schemes mentioned previously (standing unbalance due to differences in the windings and CT errors).

The difference between the negative-sequence differential scheme and the traditional split-phase scheme is that instead of only having to deal with the errors of two CTs and two windings, this scheme has to deal with the errors of six CTs and differences between six windings.

Section VIII discusses ways to reduce the impact of the standing unbalance on this and other schemes. Section IX presents methods whereby this scheme, as well as the others discussed in this section, can be secured during external faults.

4. MEASUREMENT METHODS FOR SPLIT-PHASE PROTECTION

Three methods for measuring the split-phase current are in common use. These include the following:

- Separate differentially connected CTs.
- Single-window, core-balance CT.
- Dual-window, core-balance CT.

This section reviews basic characteristics of each of these measurement techniques, pointing to their advantages and limitations. Section VII introduces a new measurement method.

4.1. SEPARATE DIFFERENTIALLY CONNECTED CTs

With reference to Fig. 14, two CTs are connected in parallel in a differential fashion, so the current in the sensing path (split-phase overcurrent relay) is a difference of the two secondary currents.

For small machines, the two CTs can be included in a single assembly with just the differential secondary terminals brought out. For larger machines, the two CTs may be installed as separate assemblies. This application has an advantage of keeping the primary conductors straight and in parallel.

However, each secondary winding must be rated for carrying half of the full-load current. As a result, the ratio (number of secondary turns) cannot be too low or else the secondary current in each winding will be high. This limits the sensitivity of this measurement method.

Also, the accuracy is limited by differences in the magnetizing characteristics of the two cores. Each CT has its own ratio error, reflecting its own tolerances in the magnetic and winding materials. As a result, the secondary currents may be slightly different, even if the primary currents are perfectly equal. This difference appears as a spurious split-phase current, limiting accuracy. Placing the two CTs in one assembly encourages CT manufacturers to match the magnetizing characteristics of the two cores for better accuracy.

This method can be used in two ways. In one alternative, the sensing device is connected to the paralleled secondary windings (Fig. 14). In another alternative, a sensing device can measure both secondary currents individually and derive the difference internally.

The latter method can have less accuracy because the measurement errors (linearity) of the sensing device for the two inputs can cause extra errors. These errors can further increase the spurious values in the internally derived difference between the two currents.

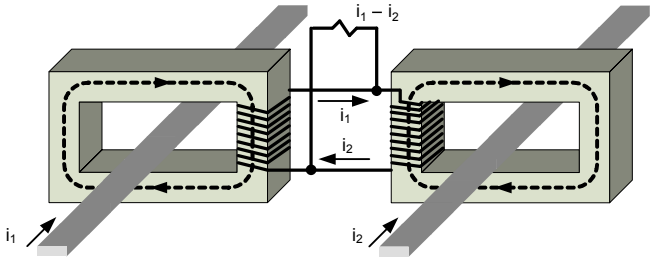

Fig. 14. Differentially connected CTs for split-phase measurement

The former method avoids this challenge and allows matching the input range of the sensing device to the expected signal level of the circulating current. Typically, a sensitive input is used to interface with the circulating current that is many times lower than the full-load current in each of the primary conductors.

4.2. SINGLE-WINDOW, CORE-BALANCE CT

With reference to Fig. 15, a single-window, single-secondary CT is used to sense the split-phase current. The two primary conductors are passed through the window in such a way that their directionality is inverted, creating opposite fluxes in the CT core and therefore allowing the common flux to cancel. As a result, the secondary winding couples only to the split-phase current.

This solution can use a low ratio (small number of secondary turns) to account for the low level of the split-phase current that is transformed into the secondary winding. This improves sensitivity and accuracy.

However, this method faces the challenge of having to route one of the primary conductors through the CT window in such a way that it produces the flux in the opposite direction (i_1 current in Fig. 15). This requirement limits the applicability of this method to smaller machines.

4.3. DUAL-WINDOW, CORE-BALANCE CT

To overcome the mechanical disadvantages of a single-window CT, a dual-window CT can be used, as depicted in Fig. 16.

In this method, the two primary conductors are parallel, but they pass through two windows of a single CT core. The sensing winding is placed on the middle limb

so that the two common fluxes cancel and the winding couples only the difference between the two primary currents (i.e., the split-phase signal). Often, a bucking winding is added to the outer limbs of the core to prevent the reactance from being somewhat high due to the secondary winding not being fully distributed around the core perimeter.

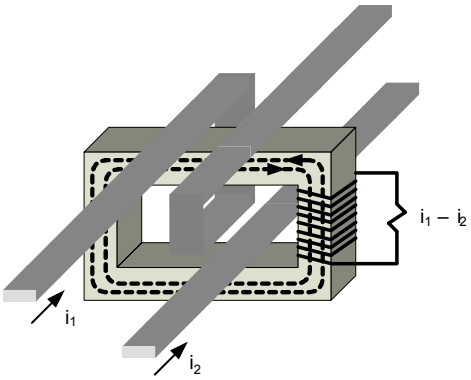

Fig. 15. Single-window, core-balance CT

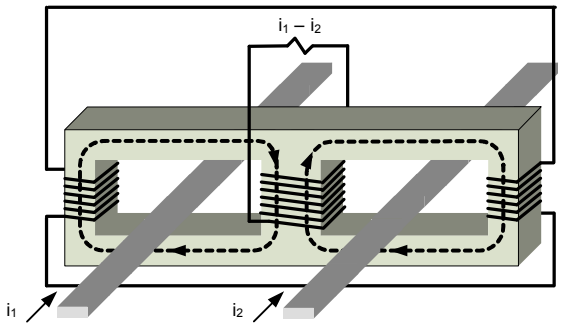

Fig. 16. Dual-window, core-balance CT

This type of CT is provided as a single assembly and offers good sensitivity and accuracy combined with relative simplicity of installation. However, the lack of a fully distributed winding makes this CT prone to errors due to external flux.

4.4. PROXIMITY ERRORS

As explained previously, split-phase protection requires measuring a relatively small difference (a few percent) between two relatively large currents.

When using two differentially connected CTs, the differences in the two magnetizing currents appear as measurement errors, as explained in Section IV, Subsection A.

Also, when using the core-balance measurement methods (single or dual window), there is a possibility of extra errors caused by proximity effects. The geometry of the core, the primary conductors, and their mutual physical positions are not perfectly symmetrical. This is particularly true when the cores are relatively small, the primary conductors are not centered, the core is oddly shaped, the primary conductors change direction soon after exiting the CT window, or other phase conductors are in close proximity to the outside edge of the CT window [4].

The presence of the magnetic core considerably reduces the impact of these factors by having the flux concentrated and guided by the core, but small differences can still occur and be projected as measurement errors, particularly in the sensitive split-phase measurements.

Placing specially selected extra compensating coils on the core is a known practice to deal with proximity errors [4].

5. SETTINGS GUIDELINES AND OPERATING EXPERIENCE WITH SPLIT-PHASE PROTECTION

5.1. PROTECTION SCHEME AND TRIP FUNCTIONS

The most commonly used scheme to detect turn-to-turn faults is the application of three individual overcurrent relays, one per phase, connected to the secondary circuit of the differentially connected CTs on the stator windings, as shown in Fig. 11. An overcurrent relay dedicated to each phase is required so that the relays can be independently set based on the magnitude of the standing circulating currents in each phase. Where a multifunction relay is applied, it is important that the integrated split-phase element allow independent, per-phase settings.

The split-phase relay operates to trip the generator breaker and initiate generator shutdown. Both instantaneous and time-overcurrent elements can be applied, as explained later in Section V.

The split-phase protection should initiate a complete shutdown process of the generator and lock itself out. This lockout feature is essential as a precautionary measure in order to not bring the generator back into service prematurely without proper inspection, because turn-to-turn faults are permanent in nature.

In addition, the split-phase protection initiates a deluge operation, because turn-to-turn faults can cause a fire due to overheating. The deluge system will trigger to spray water only if both the split-phase protection and the heat activating device operate simultaneously. It will also close louvers to starve oxygen in the generator chamber.

5.2. SELECTING SPLIT-PHASE OVERCURRENT ELEMENT SETTINGS

Ideally, no circulating currents should flow in the parallel windings of a generator stator under normal load conditions. However, as explained in Section III, due to many factors related to the winding reactance and air gap (manufacturing tolerances, ambient temperature variations, terminal voltage and load variations, and so on), there will be a finite amount of circulating current flowing in the parallel windings.

Therefore, the split-phase settings must be established based on the magnitude of standing split-phase current. This normal unbalance can also vary during the life of a generator and may not be known when the machine is initially placed in service. The settings should therefore be established after proper measurement of the circulating currents in the generator and periodically checked for security.

1) Baseline of the Standing Split-Phase Current

The existence of the circulating currents in the winding may present protection engineers with a degree of difficulty in determining proper settings. The task becomes further complicated with unequal magnitudes of the currents in all three phases.

In order to address those issues, field measurements of the currents should be conducted periodically and compared with those of the existing split-phase settings. This is because normal circulating currents continuously fluctuate, including during seasonal changes. If the magnitude of the circulating currents found from the measurements has increased significantly over time, the relay settings should be revised accordingly. Measurement of the highest split-phase current is usually found at the maximum operating voltage and current but can also occur for an unloaded machine under high voltage.

A preferred way to carry out the measurements is to take monthly readings over a reasonably long period, such as 16 months, followed by spot checks taken approximately every 6 months in the succeeding years. It is recommended to place the 6-month checks at the points when the established split-phase current reaches its minimum and maximum over its repetitive cycle. The recording is to be taken with a multimeter that is calibrated to accuracy. Preferably, the same meter should be used throughout the measuring period. Figure 17 shows a graph of typical split-phase current fluctuation over a period of 16 months.

2) General Settings Considerations

Ideally, the split-phase overcurrent element is set to detect a single shorted turn. From the sensitivity point of view, the generator manufacturer should be consulted to provide data on the value of the minimum split-phase current for a single shorted turn (typically about 4 percent of the generator full-load current).

From the security point of view, a three-phase fault test can be conducted at reduced voltage to determine the maximum standing split-phase current under external

fault conditions. The split-phase current under the normal voltage can be determined through linear extrapolation to full-load voltage. This technique is useful to assess the transient split-phase current that originates from within the machine because of differences in the branch reactances. However, this technique will likely not uncover the spurious current due to CT errors because the CTs may not saturate during the reduced-voltage short-circuit test.

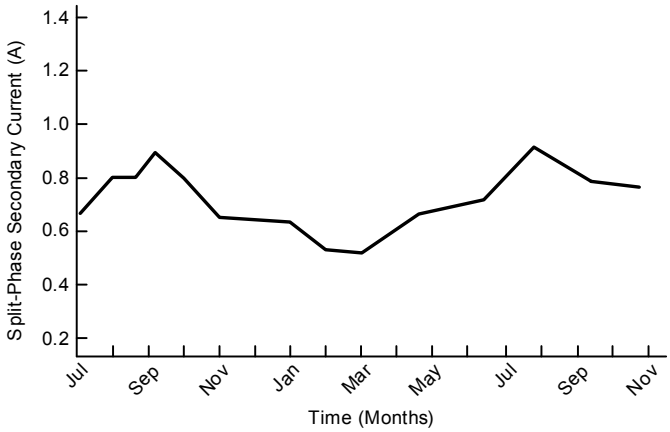

Fig. 17. Typical seasonal variation of split-phase standing current on a hydrounit

The standing split-phase currents that exist in all three phases under normal load conditions should be reasonably close to each other, unless the machine operates with a bypassed coil. In this case, the same minimum pickup setting can be applied for all three phases, based on the highest measured split-phase currents.

If, however, one of the split-phase currents is unusually high compared with the other two phases, individual phase settings should be considered.

Typically, this is the case when temporary repairs take place. After a stator coil failure, the operation staff is under pressure to bring the generator back into service with its failed coil removed or bypassed. Running the machine with one less coil will cause further voltage unbalance between the parallel windings, leading to an additional increase of the circulating currents. This will also have a further adverse effect upon the split-phase protection settings, further decreasing the sensitivity of the protection. Therefore, it is recommended that the impact of a coil removal on the generator, as well as the protection settings, be carefully weighed. Often, the pickup setting must be increased significantly on the phase that includes the bypassed coil.

3) Split-Phase Time-Overcurrent Element Settings

The pickup level should be selected to account for the maximum standing split-phase current, with margin. Guidelines for establishing the maximum standing split-

phase current were provided previously in this section. Because the split-phase currents can change over time, a margin of 50 percent is typically applied (the pickup is 150 percent of the maximum standing current) in order to ensure the element is secure until the next inspection of the standing split-phase current.

Selection of the time setting should be based on ensuring stability during external faults. The time delay of 0.5 second at twice the pickup is considered sufficient to effectively time-coordinate with close-in external faults that can cause spurious split-phase current readings due to CT errors and differences in branch reactances. For example, the IEEE Moderately Inverse (U1) Curve, as shown in Fig. 18, is chosen with the time dial set to 0.65 to achieve the aforementioned desired time-delay setting of 0.5 second.

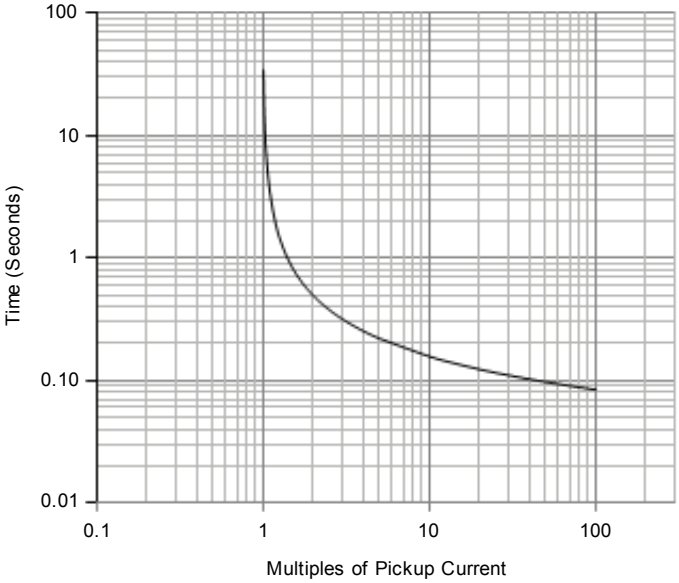

Fig. 18. IEEE moderately inverse-time characteristic applied to a split-phase time-overcurrent element

Some close-in, three-phase external faults can be severe enough that an unwanted split-phase protection operation can occur. In cases where these faults are not cleared before the split-phase protection times out, the setting can be increased to three to four times the standing split-phase current to avoid such misoperation.

Some split-phase elements can also be vulnerable to the presence of inrush currents during a dead bus synchronization, where a transformer is suddenly energized by closing a generator synchronizing breaker.

If a microprocessor-based relay is installed for protection, it is a good practice to select filtered magnitude as the operating signal (not the true RMS [Root-Mean-

Square]) in order to reduce the impact of harmonics and dc offset present in the inrush and external fault currents. Also, a momentary application of a different settings group with the higher timing can be implemented to avoid a misoperation when energizing the unit transformer.

4) Split-Phase Instantaneous Overcurrent Element Settings

Without the advantage of waiting through the external fault current, the pickup setting for the instantaneous split-phase element should be based on the highest possible value of the split-phase current. This transiently highest value occurs in conjunction with the subtransient external fault current, which, in turn, may reach up to several times the full-load current.

The resulting split-phase currents for this external fault under the worst conditions can transiently reach a value of five to seven times the standing split-phase current. According to one practice, the pickup setting can be selected as seven times the highest standing split-phase current.

When set that high, the instantaneous split-phase element will likely not detect a single-turn fault. It will instantaneously detect faults that include several turns and will provide backup protection to the generator differential protection.

6. CT SELECTION RULES

This section is focused on the selection criteria for split-phase protection with differentially connected CTs, as shown in Fig. 19.

We assume a split-phase protection application with the parameters shown in Table 1 and illustrate the process for CT selection using this example.

6.1. CT RATIO

The nominal generator current is calculated at 2.719 A. Because there are four parallel branches, the impedance of each branch (Z_{BRANCH}) may be approximated as four times the leakage reactance, or 1.758 Ω primary. The impedance of a single turn (Z_{TURN}) is 1.758 Ω/(4 • 33), or 13 mΩ primary. The voltage across a single turn is as follows:

$$V_{TURN} = \frac{\text{Nominal ph-n Voltage}}{\text{Number of Coils} \cdot \text{Turn per Coil}} = \frac{13.8\,\text{kV}}{\sqrt{3} \cdot 4 \cdot 33} = 60.4\,\text{V} \tag{10}$$

The circulating current (I_{CIR}) that flows because of a single shorted turn can be approximated as the following:

$$I_{CIR} = \frac{V_{TURN}}{Z_{BRANCH} - Z_{TURN} + \dfrac{Z_{BRANCH}}{\text{Number of Circuits} - 1}} = \frac{60.4\ \text{V}}{1.758\ \Omega - 0.013\ \Omega + \dfrac{1.758\ \Omega}{4-1}} = 25.912\ \text{A primary} \tag{11}$$

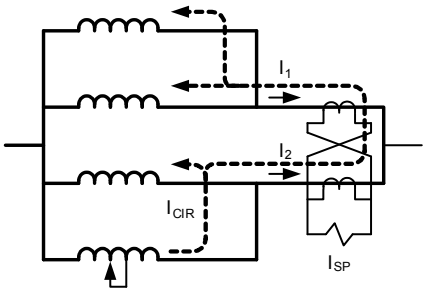

Fig. 19. Split-phase protection application for machines with four branches in parallel – relationship between the split-phase current and the circulating current

Table 1. Example system parameters

Nominal power	65 MVA
Nominal voltage	13.8 kV
System X/R	30
Subtransient reactance	0.38 pu
Leakage reactance	0.15 pu
Number of parallel circuits	4
Number of coils	33
Turns per coil	4
Split-phase element minimum pickup	0.25 A secondary

The split-phase current will be as follows:

$$I_{SP} = \frac{\text{Number of Branches} \cdot I_{CIR}}{\text{Number of Branches} - 1} = \frac{4 \cdot 25.912\ \text{A}}{3} = 34.519\ \text{A primary} \tag{12}$$

Each CT sees half of the nominal rated current under load conditions. Therefore, a CT with a ratio of 1500/5 would produce a split-phase current of the following:

$$34.519\ \text{A} \cdot \frac{5}{1500} = 0.115\ \text{A secondary} \tag{13}$$

This is less than the minimum pickup of the split-phase element. Choosing a CT with a nonstandard secondary rating of 15 would allow the element to detect a single shorted turn.

6.2. CT CLASS

The CT connection is at risk for an external, close-in phase-to-phase or three-phase fault. The generator contribution is limited by *Xd″*, and the system *X*/*R* ratio will be large. Consequently, the general rules for differential CT selection should be applied, including the following:

- Use a CT with a fully distributed secondary winding, and connect to the full winding ratio.
- Select CTs with matching characteristics (i.e., the same manufacturer, excitation curve, and internal resistance).

Select CTs with the highest practical knee-point voltage. The required voltage for saturation-free operation is given by the following:

$$V_k > (1 + X/R) \cdot I_S \cdot Z_S \tag{14}$$

where:

I_S is the secondary current for a three-phase fault,

Z_S is the one-way lead resistance up to the parallel connection (not including the return path) plus the CT internal resistance.

Returning to the example, a three-phase fault just outside the differential zone would produce a fault current of 7.156 A primary. Each CT would see 71.5 A. Assuming a CT internal resistance of 0.1 Ω and a lead resistance of 0.1 Ω, then the knee-point voltage required for saturation-free operation is as follows:

$$V_k > (1 + 30) \cdot 71.5\ \text{A} \cdot 0.2\ \Omega = 443\ \text{V} \tag{15}$$

If saturation cannot be avoided, then it must be dealt with using the methods described in Section IX.

7. NEW MEASUREMENT METHOD FOR SPLIT-PHASE PROTECTION

7.1. THE MEASUREMENT PRINCIPLE

The task is to measure small differences between two currents (i_1 and i_2). It is therefore convenient to represent the two currents with common (COM) and unbalance (UNB) components, as follows:

$$i_1 = i_{COM} + i_{UNB} \tag{16}$$

$$i_2 = i_{COM} - i_{UNB} \tag{17}$$

In other words, the two components are the following:

$$i_{COM} = \frac{1}{2}(i_1 + i_2) \tag{18}$$

$$i_{UNB} = \frac{1}{2}(i_1 - i_2) \tag{19}$$

The unbalance component (19) is simply half of the split-phase current and therefore is of interest for split-phase protection.

Referring to the example in Section VI, the above currents under load conditions and a single-turn fault would be as follows: i_1 = 1,366.33 A primary, i_2 = 1,352.67 A primary, i_{COM} = 1,359.50 A primary, and i_{UNB} = 6.825 A primary.

For simplicity, we continue using the term "split-phase current" instead of the unbalance current and rewrite (16) and (17) as follows:

$$i_1 = i_{COM} + 0.5 \cdot i_{SP} \tag{20}$$

$$i_2 = i_{COM} - 0.5 \cdot i_{SP} \tag{21}$$

The new measurement method stems from the idea to force the common and split-phase currents into separate secondary windings, each having a different ratio adequate for the level of the common and unbalance currents.

With reference to Fig. 20, two CTs are used. The primary conductors are placed in parallel through each of the windings with the advantages of easy installation and the possibility of having the two CTs as independent assemblies.

The two primary currents are represented by the common and split-phase components. These components induce the common and split-phase fluxes in the two cores.

Each CT is equipped with two secondary windings having N_{COM} and N_{SP} number of turns, respectively.

The common windings (N_{COM} turns) are connected in such a way that they only couple with the common flux, and therefore, only the common current can flow in the

N_{COM} circuit. Because of the way the two windings are connected, it is impossible for any split-phase current to flow in this circuit. The N_{COM} connection is simply open-circuited for the split-phase current.

The split-phase windings (N_{SP} turns) are connected in such a way that they only couple with the split-phase flux, and therefore, only the split-phase current can flow in the N_{SP} circuit. Because of the way the two windings are connected, it is impossible for any common current to flow in this circuit. The N_{SP} connection is simply open-circuited for the common current.

If the N_{COM} circuit were the sole connection in the scheme of Fig. 20, the scheme would be technically deficient by not allowing the path for the split-phase current and flux.

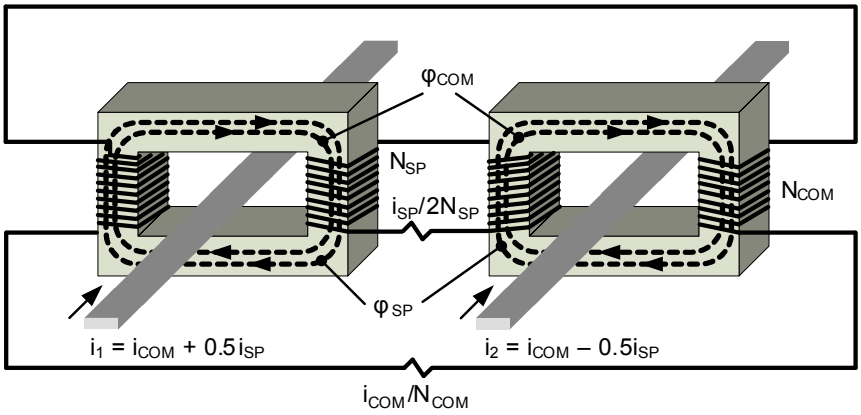

Fig. 20. Dual-ratio CT connection

Similarly, if the N_{SP} circuit were the sole connection in the scheme of Fig. 20, the scheme would be technically deficient by not allowing the path for the common current and flux.

As a system, however, the two circuits constitute a technically valid connection, forcing the large common component to couple into the high-ratio N_{COM} loop and the small split-phase component to couple into the low-ratio N_{SP} loop.

As a result, the two currents of interest are measured with adequate ratios, sensitivities, and signal ranges.

We refer again to the example of Section VI and assume N_{COM} = 300 (1500/5). If so, the common secondary current reads 1359.5/(300) = 4.532 A secondary. This current can be used for metering or short-circuit protection functions. Assume further that N_{SP} = 20. If so, the split-phase secondary current during a single-turn fault reads 13.65 A primary/(2·20) = 0.341 A secondary. This is well within the sensitivity and settings range of the split-phase protection element assumed in the example of Section VI.

The common loop can supply a device that requires measuring the common current component or can just be short-circuited to facilitate the split-phase current measurement with a low ratio for sensitivity.

The split-phase component loop can supply a sensitive input device that requires measuring the split-phase current component.

A single device can measure both the common and split-phase components, with two inputs having adequate input ranges. Such a device can respond to each of the components individually and, subsequently, derive the original conductor currents using (20) and (21).

7.2. ADVANTAGES

The new method has the following advantages:

- The same CT assembly can be used to measure the common and split-phase current components. Effectively, this scheme is a dual-output, dual-ratio CT.
- The split-phase current is measured with a low ratio, accounting for the low level of the signal. This allows the reduction of sensitivity requirements for the relay inputs.
- Mechanical mounting is simple, with the primary conductors in parallel and an option to use two separate assemblies for each of the conductors.
- The CT can be manufactured with a fully distributed winding, significantly reducing proximity effects.

The accuracy of the measurement is comparable with the differentially connected CT method.

8. ADDRESSING THE INHERENT UNBALANCE BETWEEN PARALLEL WINDING BRANCHES

As mentioned in Section II, limitations in stator manufacturing and temporary repairs result in a non-zero value of the split-phase current. This standing current (inherent unbalance) is known to vary in many machines. This variation correlates with changes in terminal voltage and loading of the machine. The correlation with loading is particularly strong in machines operated with bypassed coils [2]. Certain machines also display seasonal or daily split-phase current variations, which evidently are temperature related.

The consequence of these variations is that field measurements must be carried out over an extended period of time in order to determine a secure pickup setting and these measurements need to be rechecked on a regular basis, as explained in Section V.

Section VI illustrated the small change in split-phase current due to a single shorted turn. Consequently, applying higher settings required for machines that experience large current variation can result in significantly desensitized protection.

In a microprocessor-based relay implementation, it is possible to track this variation and remove it from the operating signal, thereby restoring the sensitivity of the element. Figure 21 presents one such algorithm.

The offset value (I_{OFF}) is calculated as follows:

- A weighted average is carried out using the current value of I_{SPM} and the previous value of I_{OFF}. Figure 22 shows a simplified flow chart for this operation.
- However, if the RESET input is asserted, then I_{OFF} takes the value of the split-phase current magnitude (I_{SPM}), effectively resetting the offset calculations. This is necessary for events for which a known change in the split-phase current occurs, such as when the generator breaker opens.

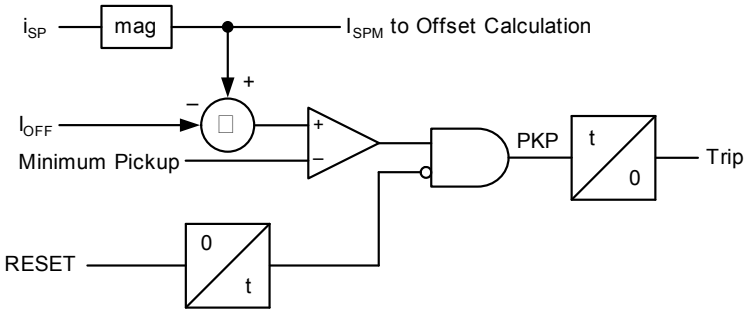

Fig. 21. Adaptive split-phase overcurrent element

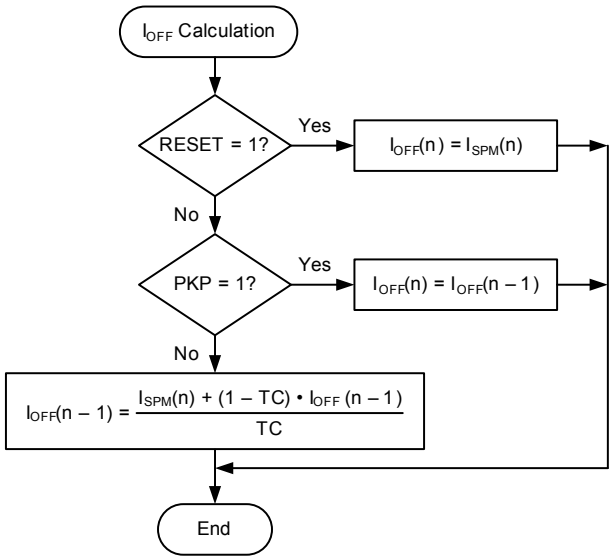

Fig. 22. Offset calculations for the algorithm of Fig. 21

- Furthermore, if PKP asserts, then I_{OFF} is not updated. This is to prevent the algorithm from adapting to the change in split-phase current due to a fault before the trip timer has a chance to time out.

The variable TC is a time constant, which determines how quickly the offset calculation tracks the split-phase current (a relay calibration setting or a user setting). Figure 23 illustrates how the offset calculation responds to an arbitrary step change in the split-phase current.

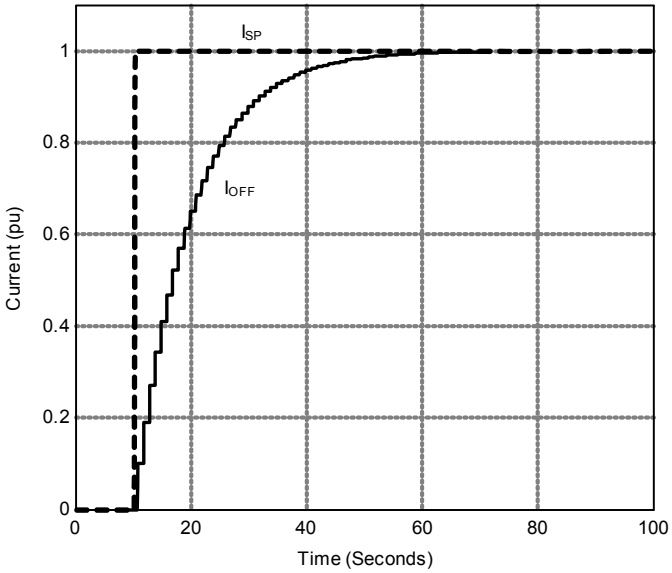

Fig. 23. Offset calculation response to a step change in the split-phase current (TC = 10 seconds)

The presented algorithm tracks the magnitude of the split-phase current. An alternative approach is to track the phasor (complex) value of the split-phase current. The approach would benefit from the ability to detect changes in angle, as well as magnitude. However, the phasor approach could be exposed to false operation for a step change in angle due to a change in system frequency because an error in frequency tracking produces a rotating phasor. Because the impedances of the stator circuit are homogeneous, magnitude tracking is considered just as effective and potentially more secure.

A potential weakness to the approach lies in the possibility of a fault that produces a change in current that is less than the selected pickup setting. In this case, the algorithm would adapt to the fault current and remove it from the operating signal. As a consequence, the pickup must be set to less than that expected for a single shorted turn. The element should also operate in parallel with a conventional (nonadaptive) split-phase overcurrent element. The conventional element operates for multiturn faults and acts as a backup to the adaptive function.

9. SECURING SPLIT-PHASE PROTECTION

9.1. SECURITY OF SPLIT-PHASE PROTECTION ELEMENTS

In all the discussion regarding split-phase protection so far, we see that all the schemes have to deal with the same issue of a natural standing split-phase current resulting from the differences in the stator windings and the different performances of the CTs in the scheme under normal operating conditions. During an external fault, an additional transient difference current is produced. This transient current is due to the following two phenomena.

First, a circulating current transient is produced in the primary circuit. The magnitude is dependent on the incidence angle of the external fault and on the characteristics of the damper winding. In machines without a damper winding, this current can be two to three times larger than the quiescent split-phase current and can take up to 30 cycles to decay.

Second, if differentially connected CTs are used to measure the split-phase current, then a difference in the CT characteristics during the fault, including CT saturation, will result in a spurious split-phase current.

Protection engineers select the primary current rating of CTs used in split-phase protection schemes based on the full-load current rating of the winding, typically 25 times higher than the circulating current produced during a turn-to-turn fault (see Section VI). By doing this, they trade sensitivity for security during external faults. However, due to the long decay of the dc current produced during an external fault, the CTs may end up saturating. Both CTs will not saturate to the exact same degree, and as a result, a difference current occurs (Fig. 24) and may result in inadvertent operation of the scheme. In applications for machines with low-impedance damper windings and differentially connected CTs, protection engineers delay the operation of the split-phase protection element, typically by up to 30 cycles, in order to prevent misoperation.

By delaying the element by up to 30 cycles, the scheme is secured from inadvertently operating during external faults, but at the same time, the protection is delayed by 30 cycles for a genuine turn-to-turn fault. In the next subsection, we discuss a new innovative method using external fault detection logic that secures this type of protection scheme during external faults without the need of an additional time delay.

9.2. EXTERNAL FAULTS AND THE ROLE OF AC AND DC EXTERNAL FAULT DETECTION

Several microprocessor-based relays have been developed that make use of an external fault detector to provide additional security for a differential element during external faults. Because the split-phase element is also at risk under the same circum-

stances, it makes sense to employ the same logic to secure the split-phase element. In a multifunction generator relay, the logic can be shared by both functions.

External fault detectors employed within differential relays often are designed to detect two types of CT saturation:

- High-magnitude external faults, which can cause saturation due to the large ac component of the current.

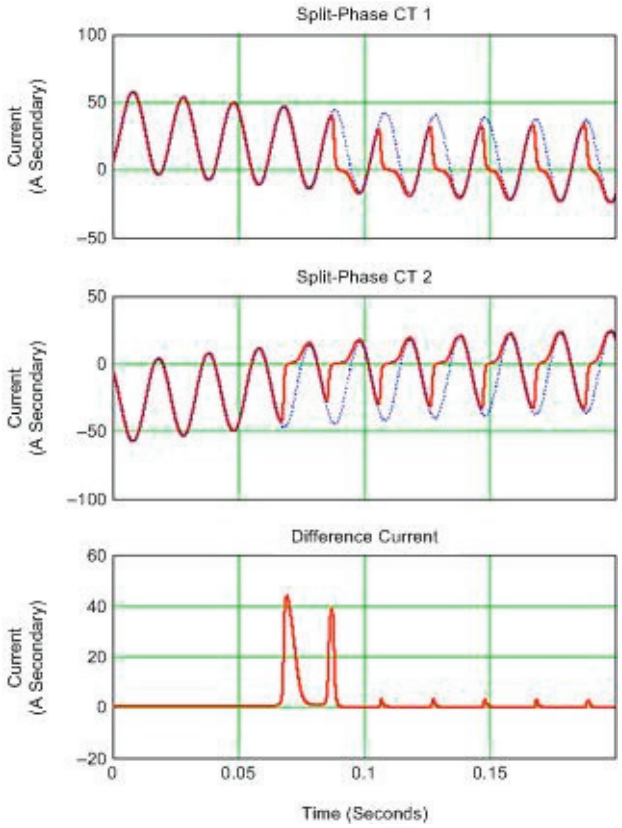

Fig. 24. Unequal saturation of the CTs in a split-phase protection scheme resulting in a fictitious differential current

- Low-magnitude external faults in which a decaying dc component with a long time constant is responsible for CT saturation.

During a heavy external fault, the CTs are initially expected to provide at least a half cycle of saturation-free operation. The ac path therefore looks for a step increase in the restraining current (I_{RST}) that is not accompanied by a corresponding increase in the differential current (I_{DIF}). Fig. 25 shows the simplified logic diagram of the ac external fault detection logic.

For detecting low-magnitude external faults that have long-decay dc signal content, the dc path compares the fundamental frequency current magnitude (I_{AC_MAG}) with the dc component current magnitude (I_{DC_MAG}), as shown in Fig. 26. A significant dc component is declared if the dc component is greater than a certain portion of the CT nominal rating or the ac component at the time. An external fault is declared if the current contains a significant dc component, if the differential current (I_{DIF}) is low compared with the restraint current (I_{RST}), and if this situation persists for several cycles.

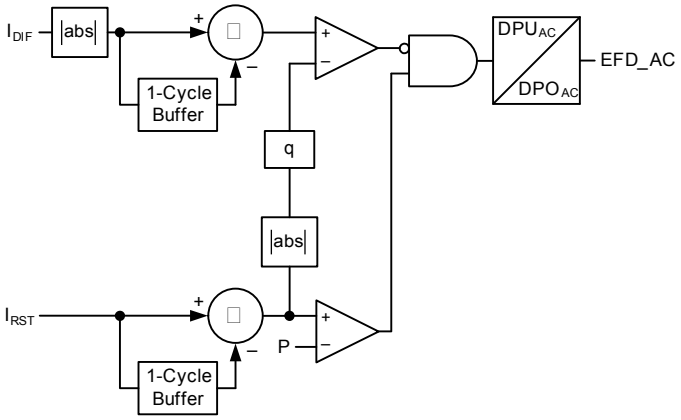

Fig. 25. AC external fault detection logic

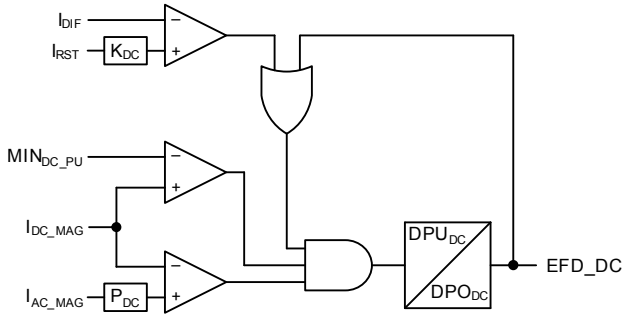

Fig. 26. DC external fault detection logic

The outputs from the ac and dc external fault detection logic are connected together with an OR gate to provide one external fault detection element. The external fault detector has significant advantages compared with a simple delay because it allows instantaneous operation for internal faults and relieves the protection engineer of the task of determining an optimal delay setting. It addresses the problem of spurious

split-phase currents that arise from the response of the machine or from the performance of the CTs.

9.3. OPEN CT DETECTION

So far, we have discussed methods of increasing the sensitivity of turn-to-turn protection elements and securing them during external fault conditions. However, how do we secure these schemes from misoperating when a CT is either inadvertently open- or short-circuited? The answer to this question lies in what type of protection scheme is employed to provide the turn-to-turn protection.

If a standalone split-phase protection scheme (comprised of two differentially connected CTs with one of these CTs open-circuited) is used, the scheme would be subjected to the load current of the winding (in A secondary). By simply using the information provided by these two CTs, there is no way to distinguish if this is due to a genuine internal fault or if there is trouble associated with one of the CTs in the scheme. If a microprocessor-based relay is used in implementing the scheme, it is likely that the differential protection scheme will also be realized in this relay. If this is the case, part of the ac external fault detection logic could be used to secure the split-phase protection element, as shown in Fig. 27.

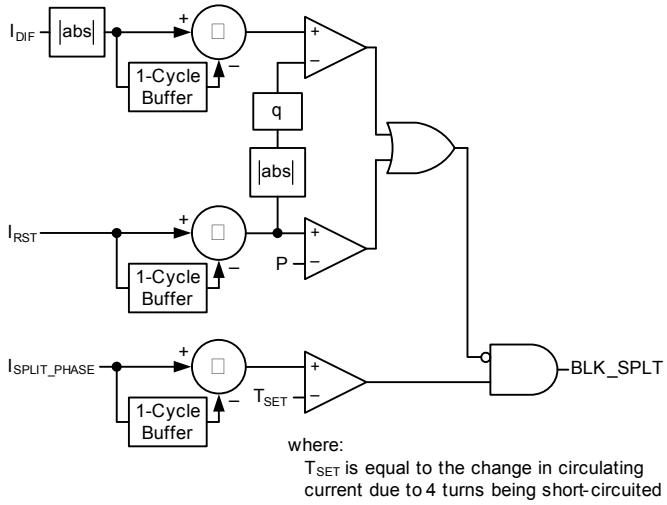

Fig. 27. Security logic for preventing inadvertent operation of the split-phase protection element due to an open-circuited CT

Note that if the machine is lightly loaded and one of the CTs in this scheme is open-circuited, it will not be possible to detect this condition; similarly, if one of the CTs is short-circuited, this will also not be detected.

If turn-to-turn protection is realized by using the combined differential and split-phase protection scheme or the negative-sequence differential scheme, then detecting an open- or short-circuited CT is possible. The open-circuited CT logic is performed on a per-phase basis and functions as follows. The logic calculates both the restraint and difference currents. A troubled CT condition is declared if the increase in the differential current is equal to the decrease in the restraint current.

Adaptive split-phase protection that removes the standing split-phase current from the operating signal is more sensitive (Section VII). When supervised with the external fault detection logic and open CT detection logic (Section VIII), the split-phase protection elements are also more secure. In this way, better performance is achieved by relying on time delay or elevated pickup thresholds, without extensive engineering effort for the calculation of settings.

10. CONCLUSION

Turn-to-turn faults are possible in stator windings with coils made up of multiple turns in the same slot. Undetected, these faults can cause considerable damage before evolving into phase or ground faults. It is desirable to detect these faults and trip the machine in the typical short-circuit protection time frame (fraction of a second).

Split-phase protection takes advantage of the parallel configuration of hydromachine windings to detect turn-to-turn faults, as well as other fault types. However, achieving adequate sensitivity without jeopardizing security is a challenge. This is mainly due to the normal practice of using differentially connected CTs to measure the split-phase current.

In this paper, we present the underlying principles of split-phase protection, review methods for split-phase current measurement, and identify potential measurement errors. The paper identifies the mechanisms that produce transient split-phase currents during external faults.

We review existing methods of split-phase protection and offer settings guidelines and rules for CT selection.

We describe a novel method for the measurement of split-phase current. The method promises to provide the improved sensitivity of a core-balance CT and, at the same time, the ease of installation of differentially connected CTs.

The paper presents a new method for addressing the inherent unbalance in the stator currents, which results in a standing split-phase current without the need to desensitize the split-phase element or risk misoperation on external faults.

The paper reviews methods to secure split-phase protection during external faults and describes an improved method to provide security without sacrificing operation speed or sensitivity for internal faults. Future work is envisioned to implement these methods into a microprocessor-based relay and to carry out field trials.

REFERENCES

[1] DeHAAN J., *Electrical Unbalance Assessment of a Hydroelectric Generator With Bypassed Stator Coils*, proceedings of the IEEE International Conference on Electric Machines and Drives, Seattle, WA, May 1999.

[2] FINNEY D., KASZTENNY B., Mc CLURE M., BRUNELLO G., *Self-Adaptive Generator Protection Methods*, Proceedings of the IET 9th International Conference on Developments in Power System Protection, Glasgow, United Kingdom, March 2008.

[3] *IEEE Tutorial on the Protection of Synchronous Generators*, 1995.

[4] JONES K.W., *Addressing Window Type Transformer Proximity Errors*, Proceedings of the 59th Annual Conference for Protective Relay Engineers, College Station, TX, April 2006.

[5] RHUDY R.G., SNIVELY H.D., WHITE J.C., *Performance of Synchronous Machines Operating With Unbalanced Armature Windings*, IEEE Transactions on Energy Conversion, Vol. 3, No. 2, pp. 391–397, June 1988.

[6] SILLS H.R., McKEEVER J.L., *Characteristics of Split-Phase Currents as a Source of Generator Protection*, Transactions of the American Institute of Electrical Engineers, Part III: Power Apparatus and Systems, Vol. 72, No. 2, pp. 1005–1016, January 1953.

[7] WALKER J.H., *Large Synchronous Machines: Design, Manufacture, and Operation*. Oxford University Press, 1981.

[8] Voith Hydro, *Micalastic® Insulation for High Voltage Hydro Generators*, 2009. Available: http://www.voithhydro.com

load modeling, parameter estimation,
particle swarm optimization, composite load model

Paweł REGULSKI*, Francisco GONZALEZ-LONGATT*,
Vladimir TERZIJA*

ESTIMATION OF COMPOSITE LOAD MODEL PARAMETERS USING IMPROVED PARTICLE SWARM OPTIMIZATION

Power system loads are one of its crucial elements to be modeled in stability studies. However their static and dynamic characteristics are very often unknown and usually changing in time (daily, weekly, monthly and seasonal variations). Taking this into account, a measurement-based approach for determining the load characteristics seems to be the best practice, as it updates the parameters of a load model directly from the system measurements. To achieve this, a Parameter Estimation tool is required, so a common approach is to incorporate the standard Nonlinear Least Squares, or Genetic Algorithms, as a method providing more global capabilities. In this paper a new solution is proposed – an Improved Particle Swarm Optimization method. This method is an Artificial Intelligence type technique similar to Genetic Algorithms, but easier for implementation and also computationally more efficient. The paper provides results of several experiments proving that the proposed method can achieve higher accuracy and show better generalization capabilities than the Nonlinear Least Squares method. The computer simulations were carried out using a one-bus and an IEEE 39-bus test system.

1. INTRODUCTION

Power system loads have a significant impact on the system stability. It is known that the load dynamic response is one of the key elements driving the system into dangerous voltage instability or even to catastrophic voltage collapse [3]. Some of the power systems studies, including studies of interarea oscillations, voltage stability and long-term stability, often require consideration of dynamic loads. Taking also into account that typically motors consume 60–70% of the total energy supplied by a power system, Induction Motors (IM) have become one of the crucial elements to be modeled [6]. On the other hand, due to technological progress, nowadays more and more Intelligent

* School of Electrical and Electronic Engineering, The University of Manchester, UK, e-mail: pawel.regulski@postgrad.manchester.co.uk, fglongatt@ieee.org, v.terzija@manchester.ac.uk.

Electronic Devices are deployed in power systems, including newly emerging Wide Area Monitoring Systems (WAMS), which are capable of providing huge amounts of data in real-time. To take the advantage of this fact, it seems that the measurement-based approach to Load Modeling might be a more convenient and efficient option [1], [7]–[9]. This technique is utilizing previously captured data for the purpose of estimation of load models' parameters by minimizing the difference between the measurements and the model's output. Such method can efficiently increase the quality of modeling by updating the parameters whenever inacceptable mismatch is detected.

Selection of appropriate load model is probably the most challenging task, thus it needs a special consideration. Designers have to consider which phenomena are of interest in particular case. Load being a combination of heating and lighting devices will require a model with slowly recovering power, therefore a simple Exponential Recovery Model [2] would be suitable in this case. On the other hand, when Induction Motors are the dominant element of a load mix, which is assumed to be the case in this paper, then a Composite Load Model (CLM) [1], [7], [8] should be selected. A CLM is simply an Induction Motor model supported by a Static Load (SL) model, which takes into account any non-dynamic devices. In Section II the CLM adopted in this paper will be in detail described.

Most of the dynamic load models are highly nonlinear, thus making the estimation process difficult and challenging. Traditionally, the Nonlinear Least Squares (NLS) method has been used as a basic tool for obtaining the model's parameters. However, researchers also have demonstrated a huge interest in Artificial Intelligence (AI) based methods, which could overcome the "local" limitation of the standard NLS method. So far Genetic Algorithms (GA) [7], [9] have been successfully introduced to the field of load modeling and in this paper the authors would like to propose an interesting alternative to GA, another AI technique called Improved Particle Swarm Optimization (IPSO) [5]. Both methods give similar results, however IPSO is easier for implementation and computationally more efficient. Moreover, the technique can achieve better accuracy than the NLS method, which will be demonstrated in this paper.

2. COMPOSITE LOAD MODEL

Composite Load Model is a voltage dependant dynamic model represented by an Induction Motor model connected in parallel with a Static Load model. A clear and thorough derivation of the most commonly used IM model is given in [6]. For representation in power system stability studies, stator transients are neglected, which results in the following three dynamic equations describing the *load model*:

$$\frac{dv'_d}{dt} = \frac{1}{T'_0}[v'_d + (X - X')i_{qs}] + \frac{d\theta_r}{dt}v'_q$$

$$\frac{dv'_q}{dt} = \frac{1}{T'_0}[v'_q - (X - X')i_{ds}] - \frac{d\theta_r}{dt}v'_d \tag{1}$$

$$\frac{d\omega_r}{dt} = \frac{1}{2H}(T_e - T_m)$$

and two algebraic equations representing the stator current:

$$\begin{aligned} i_{ds} &= \frac{1}{R_s^2 + X'}[R_s(v_d - v'_d) + X'(v_q - v'_q)] \\ i_{qs} &= \frac{1}{R_s^2 + X'}[R_s(v_q - v'_q) - X'(v_d - v'_d)] \end{aligned} \tag{2}$$

where *d* and *q* indices indicate the *d*-axis and *q*-axis of the *d*-*q* reference frame, respectively, *s* and *r* indices indicate the stator and rotor values, v' is the voltage behind the transient reactance, in pu, H is the motor inertia constant, in s, ω is the rotor speed, in pu, T'_0 is the transient open circuit time constant (3), in s, X' is the transient reactance (4), in pu, R_S is the stator resistance, in pu, X is a sum of the stator reactance X_S and the magnetizing reactance X_m, in pu, T_e is the electromagnetic torque, in pu, T_m is the load torque, in pu and $d\theta_r/dt$ is the slip speed (5), in rad/s.

$$T'_0 = \frac{X_r + X_m}{R_r \omega_s} \tag{3}$$

$$X' = X_s + \frac{X_m X_r}{X_m + X_r} \tag{4}$$

$$\frac{d\theta_r}{dt} = \omega_r - \omega_r \tag{5}$$

where R_r and X_r are the rotor resistance and reactance, respectively, in pu, ω_s and ω_r are the synchronous and rotor speed, respectively, in rad/s. It should be noted that in (1) ω_r is expressed in pu.

The electromagnetic and load torques are calculated as follows:

$$T_e = v'_d i_{ds} + v'_q i_{qs} \tag{6}$$

$$T_m = (A\omega_r^2 + B\omega_r + C)T_0 \tag{7}$$

where T_0 is the nominal torque at nominal speed, in pu, A, B and C donate the torque coefficients: proportional to the square of the speed, proportional to the speed and

constant coefficient, respectively. In addition the coefficients obey the following equality:

$$T_m = (A\omega_r^2 + B\omega_r + C)T_0 \tag{8}$$

The active and reactive powers are calculated as follows:

$$P_{IM} = v_d i_d + v_q i_q \tag{9}$$

$$Q_{IM} = v_q i_d + v_d i_q \tag{10}$$

The static part of the model can be described using the well known Exponential Load Model (ELM) [3]:

$$P_S = P_0 \left(\frac{V}{V_0} \right)^{\alpha} \tag{11}$$

$$Q_S = Q_0 \left(\frac{V}{V_0} \right)^{\beta} \quad Q_S = Q_0 \left(\frac{V}{V_0} \right)^{\beta} \tag{12}$$

where V_0 is the pre-disturbance voltage, in pu, P_0 and Q_0 are the pre-disturbance active and reactive power, respectively, in W and var. P_S and Q_S are the static load power demands, respectively, in W and var, α and β are the static exponents.

The total power output of the *CLM* is described as follows:

$$P_{CLM} = S_b P_{IM} + P_S \tag{13}$$

$$Q_{CLM} = S_b Q_{IM} + Q_S \tag{14}$$

where S_b is the induction machine power base, in VA.

To obtain an output from the above presented model, the following vector with 13 unknown parameters needs to be determined:

$$\theta = [H, R_s, T_0, T_0', X, X', S_b, A, B, \alpha, \beta, P_0, Q_0 \tag{15}$$

The initial values of the 3 states of the IM model, v_d', v_q' and ω_r, are obtained by solving the model with respect to the initial (pre-disturbance) voltage. Such approach reduces the dimension of the problem by 3 and therefore speeds up the convergence and increases the accuracy of the final solution.

3. PARAMETER ESTIMATION

Traditionally, to estimate the parameter vector (13) of the Composite Load Model, the Nonlinear Least Squares method has been incorporated. For this purpose the task

was formulated as a curve fitting problem in which the following *objective function* has to be minimized:

$$\min \varepsilon(\theta) = \min \frac{1}{n} \sum_{k=1}^{n} [(P_{mk} - P_{CLMk})^2 + (Q_{mk} - Q_{CLMk})^2] \tag{16}$$

where P_m and Q_m are the measured active and reactive power, respectively, in W and var and n is the number of samples simultaneously processed in the estimation process. Note that the same objective function will be used to formulate the Improved Particle Swarm Optimization below.

Originally, Particle Swarm Optimization was proposed by Kennedy and Eberhart [4] in 1995 and it was inspired by bird flocks' social behaviors. The idea of this technique is to produce a number of *particles*, which will then move around the searching space to find the best solution. The procedure of the method is depicted in a flowchart in Fig. 1.

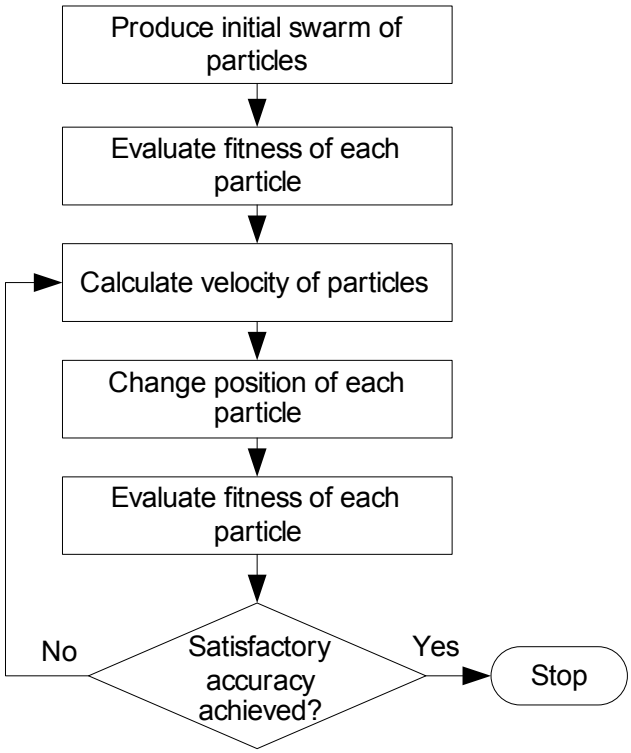

Fig. 1. Flowchart of PSO

The method starts with populating a number of particles to create a *swarm*. In fact, each particle is simply a parameter vector (13) with randomly selected values (limited

by a certain range particular to each parameter). The value of each particle indicates its *position* in the swarm, based on which a particle's *fitness* can be calculated, whereas fitness is a quantity indicating the accuracy of the solution represented by each particle. The fitness should increase with the accuracy, so to achieve this, a reciprocal of the objective function (16) is used.

To change the position of a particle its *velocity* needs to be calculated as follows:

$$V_i^{k+1} = \omega V_i^k + c_1 r_1 (P_i^k - \theta_i^k) + c_2 r_2 (P_g^k - \theta_i^k) \tag{17}$$

where V_i^k and V_i^{k+1} are the actual and next step velocity of i-th particle, respectively, ω is the inertia weight, P_i^k is the best previous position of i-th particle, P_g^k is the best global position, θ_t^k is the actual i-th particle position, c_1 and c_2 are the acceleration coefficients usually equal to 2 and r_1 and r_2 are random numbers ranging from 0 to 1.

After obtaining the velocity of a particle, the position can be updated:

$$\theta_i^{k+1} = \theta_i^k + V_i^{k+1} \tag{18}$$

The process is usually terminated after reaching either maximum number of iterations or satisfactory accuracy of the result.

The Improved Particle Swarm Optimization proposed in [5] offers an increase in both, the precision and the speed of convergence.

The improvement has been achieved by introducing a variable inertia weight ω, whereas originally it was a predefined constant. The function modulating ω is as follows:

$$\omega = \left\{ \frac{(iter_{\max} - iter)^n}{(iter_{\max})^n} \right\} (\omega_{initial} - \omega_{final}) + \omega_{final} \tag{19}$$

where $\omega_{initial}$ is the initial inertia weight, ω_{final} is the final inertia weight, $iter_{\max}$ is the maximum number of iterations, *iter* is the number of current iteration and n is the nonlinear modulation index. Inertia weight defined in such way is decreasing with each iteration, consequently reducing the contribution of previous velocity in calculating the new one. This improves the accuracy and convergence in the final stage of the estimation.

The following section provides a comparison of the introduced method against the traditional NLS.

4. SIMULATION RESULT

In order to provide the most reliable results, two case studies have been examined. The data was obtained from two separate network models built in DIgSILENT Power

Factory software. To expose the dynamics of an IM a voltage variation at the machine's terminal needs to occur, thus in the first case a voltage step change was simulated, while in the second case a fault was incepted. All the data was exported to Matlab environment at the sampling rate of 1600 Hz.

4.1. VOLTAGE STEP CHANGE

The first test network consists only of a programmable voltage source feeding a single cage IM through one busbar. The intention was to star with a simple case and a simple IM (single cage IM is a machine which can be modeled with fewest parameters, thus it should be easier to estimate its response) and then move to more sophisticated tests.

To obtain the results using NLS, the Optimization toolbox in Matlab has been used. It offers an implementation of the Levenberg–Marquardt algorithm for solving curve-fitting problems.

The methodology of presenting results in both case studies is the same: few data sets were obtained and then one set was used to estimate the parameters of the model and the others were used as cross-validation data; such test was repeated for each data set.

The first study case consist of 4 data sets obtained by simulating a step change with pre-disturbance voltage equal to 1 pu and post-disturbance voltage equal to 0.9, 0.8, 0.7 and 0.6 pu. Figure 2 presents the results IPSO (0.7 step change).

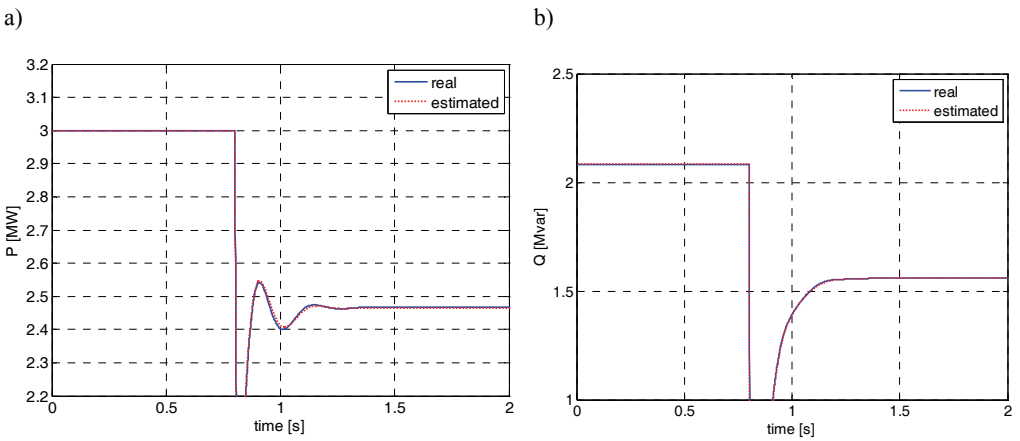

Fig. 2. Active a) and reactive b) power estimation with IPSO

The summary of this case study is given in Fig. 3. The first two bars in each experiment present the error of the estimation, whereas the remaining two bars show an average error obtained during a cross-validation test. This cross-validation technique

provides information about generalization capabilities of the model and the estimation method.

It can be clearly seen from the plots that IPSO shows better performance than NLS method. One needs to keep in mind that the total performance of a method is based on the sum of active and reactive power error, because this is how the objective function (16) is formulated. IPSO also has better generalization capabilities, which can be assessed based on the average error. What is interesting is that this average error is decreasing for higher voltage deviations, which means that more general solution can be obtained. Higher voltage step change provides more information about the speed-torque characteristic of the model, thus better result can be reached. It seem that the NLS method do not take advantage of this fact.

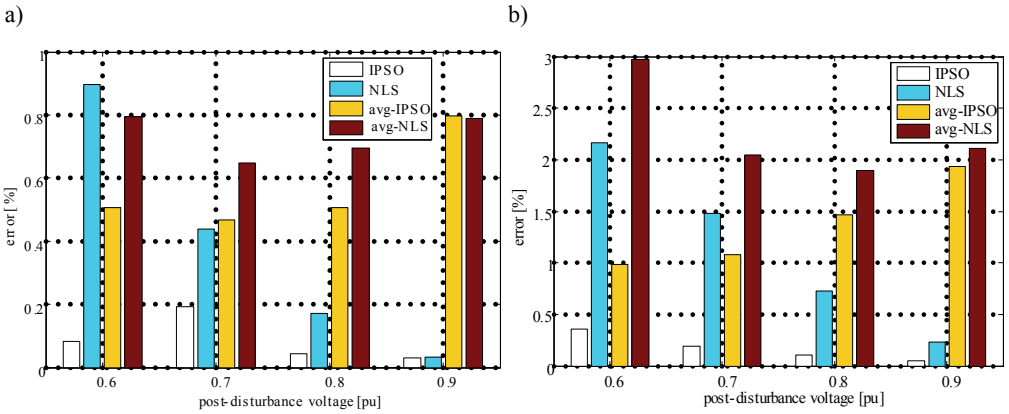

Fig. 3. Summary of active a) and reactive b) power estimation

4.2. FAULT TEST

In the second case study an IEEE 39-bus test network has been used (Fig. 4). The system provides more realistic approach also because of a double cage IM connected at bus 4. Voltage variation was caused by a fault incepted at bus 16 and lasting 0.2 s. Different data sets were obtained by setting the fault resistance to 5, 0.5 and 0.05 Ω.

Figure 5 presents results for the 5 Ω fault resistance data set and Fig. 6 provide a summary of this case study.

In this case study IPSO also shows better performance, especially in terms of reactive power error. It also has to be noted that the double cage IM is more complex then the single cage IM used in previous case. The purpose of using more complex model to produce the test data in this case was to investigate the ability of a Composite Load Model to approximate different IM, which might be an essential feature, since it is not known what kind of machines might be connected to a node in a power system.

Generalization capabilities again are considerably better in case of IPSO; the average reactive power error is always at least 3 times lower than in case of NLS. Average active power error is not so dramatically different, but still its value is lower when IPSO is used.

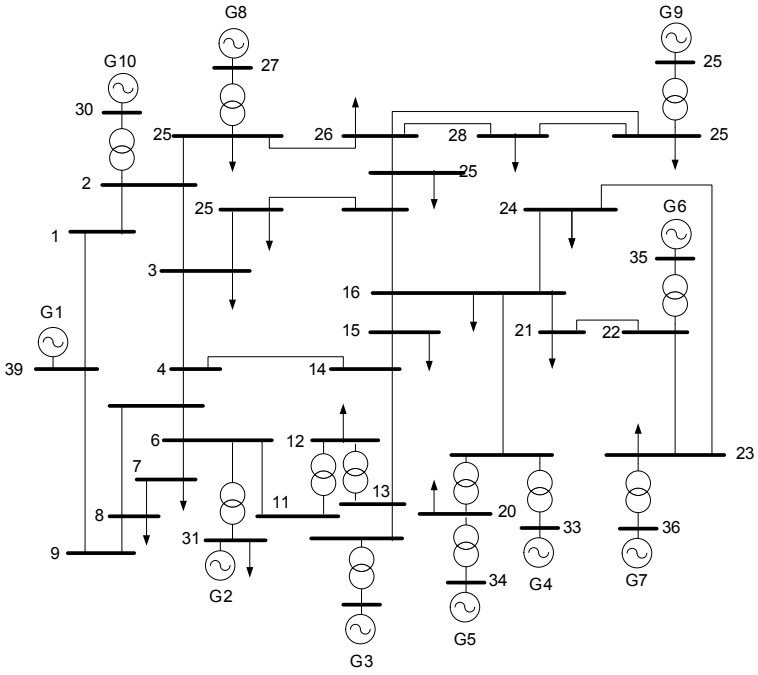

Fig. 4. Diagram of the IEEE 39-bus test system

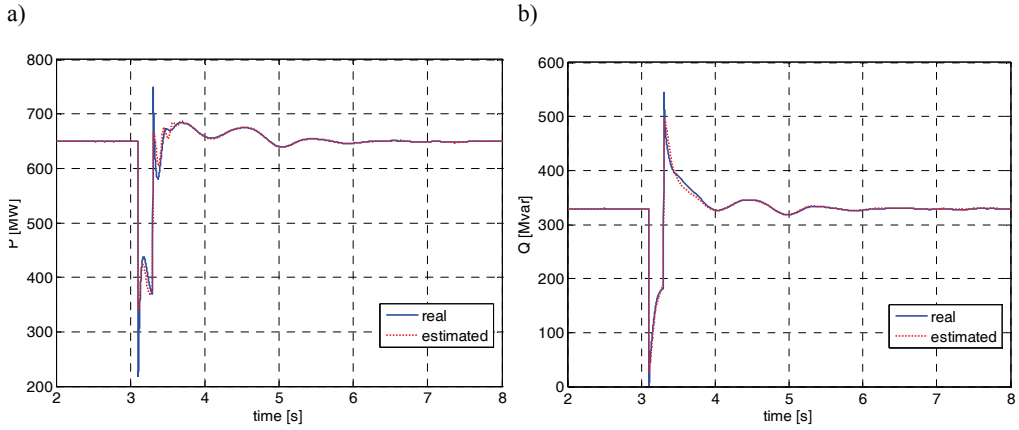

Fig. 5. Active a) and reactive b) power estimation with IPSO

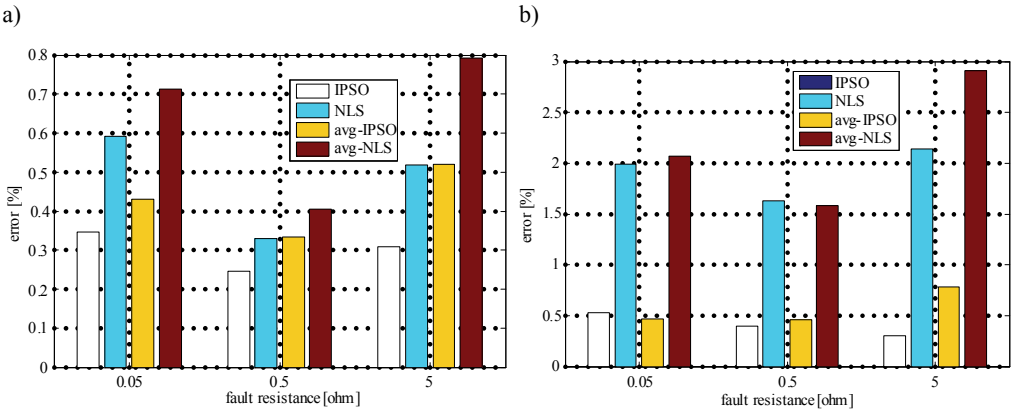

Fig. 6. Summary of active a) and reactive b) power estimation

5. CONCLUSION

In this paper the Improved Particle Swarm Optimization method is presented. It was demonstrated that it can be very practical and efficient for estimation of parameters of the Composite Load Model. It was shown that the accuracy of this new technique is very high and the cross-validation test proved its excellent generalization capabilities. Compared to the standard NLS method, the new one requires a longer computationally time, which is rather typical to Artificial Intelligence type techniques. Having in mind the availability of modern fast computers, efficient implementation of the method is not seen as an issue.

Contrary to the NLS method, the IPSO is not critical in terms of determining the starting point (initial estimate of the vector with unknown parameters). The IPSO just requires a definition of a range of the searching space, which is usually known. For the same reason the Genetic Algorithms were introduced to assist NLS in solving the problem. The idea was to use GA to find the initial guess for the NLS method, which could usually reach better accuracy in shorter time. The results presented here prove that IPSO, having the same global abilities as GA, can also give very accurate results. For offline studies IPSO can be a very good alternative to both, GA and NLS.

REFERENCES

[1] CHOI B.-K., CHING H.-D., LI Y., CHEN Y.-T., HUANG D.-H., LAUBY M.G., *Development of Composite Load Models of Power Systems using On-line Measurement Data*, Power Engineering Society General Meeting, 2006, IEEE, 2006.

[2] CHOI B.-K., CHIANG H.-D., LI Y., LI H., CHEN Y.-T., HUANG D., LAUBY M.G., *Measurement-based dynamic load models: derivation, comparison, and validation*, IEEE Transactions on Power Systems, Vol. 21, No. 3, pp. 1276–1283, Aug. 2006.
[3] CUTSEM T., VOURNAS C., *Voltage Stability of Electrical Power System*, Kluwer Academic Publishers, 1998.
[4] CUTSEM T., VOURNAS C., *Voltage Stability of Electrical Power System*, Kluwer Academic Publishers, 1998.
[5] GUANGYI C., WEI G., KAISHENG H., *On Line Parameter Identification of an Induction Motor Using Improved Particle Swarm Optimization*, Proceedings of the 26th Chinese Control Conference, 26–31 July 2007.
[6] KUNDUR P., *Power System Stability and Control*, McGraw-Hill, 1994.
[7] MA J., DONG Z.-Y., HE R.-M., HILL D.J., *Measurement-based Load Modeling using Genetic Algorithms*, IEEE Congress on Evolutionary Computation, 2007, CEC 2007, pp. 2909–2916, 25–28 Sept. 2007.
[8] MAITRA A., GAIKWAD A., POURGEIK P., BROOKS D., *Load Model Parameter Derivation Using an Automated Algorithm and Measured Data*, Power and Energy Society General Meeting – Conversion and Delivery of Electrical Energy in the 21st Century, 2008, IEEE, 20–24 July 2008, pp. 1–7.
[9] WEN F J.Y., JIANG L., WU Q.H., CHENG S.J., *Power System Load Modeling by Learning Based on System Measurements*, IEEE Transactions on Power Delivery, Vol. 18, No. 2, April 2003, pp. 364–371.

local voltage stability, reactive power compensation,
load shedding, transformer tap control

Bartosz BRUSIŁOWICZ*, Janusz SZAFRAN*

VOLTAGE AND LOCAL STABILITY MARGIN REGULATION OF THE RECEIVING NODE

Regulation methods of the receiving node voltage has been analyzed in the paper. There has been used Thevenin equivalent to develop, simulate and analyze these methods. The paper presents also an on-line method of Thevenin model parameters updating using local phasor measurements. Based on this model influence of the voltage regulation on the local stability margin of the receiving node has been analyzed. Three methods of voltage regulation: transformer tap changing, compensation of reactive power and under voltage load shedding have been examined.

1. INTRODUCTION

A lot of occurrences in power system can influence voltage level and local stability margin at the receiving node. The most significant are power system configuration and node load changes. Incorrect reaction of power system control in such cases can lead to disturbance or even blackout; therefore it is important to take intelligent actions to maintain voltage and simultaneously stability margin at the acceptable level. To study the safety of node there may be used a simplified Thevenin equivalent model. Parameters of this model can be calculated and updated using local measurements, so it is possible to apply the model in substation automation. Voltage level and stability margin depend on parameters of Thevenin model seen from receiving node as well as on the parameters and type of load. The node voltage and stability margin can be maintained by use of: transformer tap changer, reactive power compensation and in extreme cases load shedding. In the paper the influence of the above mentioned methods of voltage control on local stability margin for different types of load is analyzed and simulated.

* Institute of Electrical Power Engineering, Wrocław University of Technology, Wrocław, Poland.

2. THEVENIN EQUIVALENT

To analyze power flow in the power system there is used a model containing complete information about the current system configuration and its parameters. Assuming the symmetry of loads and generators, the model can be considered as a single-phase one. For analysis of influence of voltage regulation on local stability margin simplified Thevenin model may be used (Fig. 1).

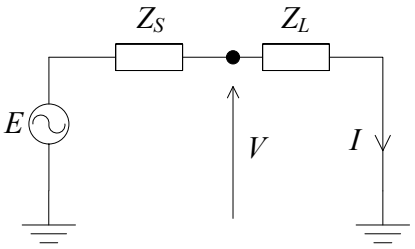

Fig. 1. Simplified Thevenin equivalent

Thevenin equivalent consists of: ideal voltage source E, series system impedance Z_S and load model Z_L. This circuit may be defined by following formulas:

$$V = \frac{E}{\sqrt{1 + 2W\cos\beta + W^2}} \tag{1}$$

$$S = \frac{E^2}{Z_S}\frac{W}{1 + 2W\cos\beta + W^2} \tag{2}$$

where: V – node voltage, S – load apparent power, E – ideal source voltage, Z_S – series system impedance, $W = Z_S/Z_L$, $\beta = \varphi_S - \varphi_L$, φ_S and φ_L – system and load impedance phase angles, respectively.

In the Thevenin model values of parameters E, Z_S and Z_L can fluctuate. Impedance Z_S corresponds to actual power system configuration. Actions that change value of this impedance are the inclusions and exclusions of power system components like power lines and transformers. Changes are significant especially when connections occur close to the considered node. Value of Z_S is not directly measurable. However method described below to calculate and update of value of this impedance can be used. Considering the voltage changes it is assumed that the node is connected to strong power system and changes of voltage source E are insignificant. So, constant value of E can be assumed. Changes of load impedance Z_L cause changes of received apparent power and value of actual node voltage. Decrease of voltage provokes voltage regulation actions. Tap changer regulation change not

only value of load but also the load impedance seen at the high voltage terminals of the transformer. Frequently it causes decrease of the local stability margin. Conditions are different with compensation of reactive power, which increase voltage level and the stability margin. In extreme case of voltage decrease load shedding ought to be initialized. To determine actual stability margin Z_S value should be calculated and load impedance Z_L should be measured.

2.1. THEVENIN MODEL ON-LINE ACTUALIZATION

Changes in power system configuration affect the fluctuation of Thevenin model parameters. It is continuously changing due to operations carried out in the system, such as switching or disabling the components that take place during normal operation and failures. To use model in substation automation it is necessary to make on-line actualization of value of parameters according to changes occurring in power system. Value of Z_L impedance is easily measurable. However calculations of E and Z_S are required. Method described in paper [1] can be used. Assuming that only parameters of load Z_L are changing (E, Z_S – const.) derivatives of voltage V against W parameter dV/dW and apparent power S against W factor dS/dW from equations (1) and (2) can be calculated, respectively. Dividing obtained derivatives yields:

$$\frac{dS}{dV} = -\frac{S}{V}\frac{1 - W^2\left(1 + 2\dfrac{d\cos\beta}{dW}\right)}{W\left[\cos\beta + W\left(1 + \dfrac{d\cos\beta}{dW}\right)\right]} \tag{3}$$

In case of when value of factor W is positive and contained between 0 and 1 (1 is stability limit), the value of this derivative is negative. Consequence of increase of load is increase of apparent power and decrease of node voltage. Equation (3) allows to calculate value of W factor according to:

$$W = \frac{-b\cos\beta - \sqrt{b^2\cos^2\beta - 4a\left[b(1+c) - a(1+2c)\right]}}{2\left[b(1+c) - a(1+2c)\right]} \tag{4}$$

where: $a = S/V$, $b = dS/dV$, $c = d\cos\beta/dW$.

Determining series system impedance Z_S value by calculating W from previous formula and dividing by measured Z_L value can be done. It is assumed that the Z_S, E_S and φ_S are constant between each measurement or these variations are so small that cause negligible errors in estimated values. Changes of received apparent power S and node voltage V must be caused only by load impedance changes. This term is easy to meet because changes of load impedance are much more often than changes in system configurations.

2.2. LOCAL STABILITY LIMIT

Determined parameters of Thevenin model can be used to calculate local stability margin. By using of the Thevenin model there can be proved that the maximum power transfer and also the limit of stability of receiving node occur when the following equation is true [5]:

$$\overline{V} = \left(\overline{E} - \overline{V}\right)^* \tag{5}$$

From equation (5) the impedance condition can be determined. The stability limit occurs when load impedance and series system impedance are equal:

$$\left|\overline{Z}_L\right| = \left|\overline{Z}_S\right| \tag{6}$$

For easy implementation the voltage stability margin should be restricted. Therefore, the local voltage stability margin ΔW can be described as:

$$\Delta W = 1 - \frac{|Z_S|}{|Z_L|} = 1 - W \tag{7}$$

The voltage margin indicator ΔW takes values from 0 (stability limit) to 1 (idle node).

3. VOLTAGE CONTROL OF THE RECEIVING NODE

Parameters of working point of receiving node vary according to changes in power system and changes of load. This causes changes of received active and reactive power, value of voltage and stability margin. Work at insufficient stability margin can lead to instability. In those conditions appropriate value of voltage should be maintain and demanded power should be delivered. All of this should be done in conditions of stable work of receiving node with secure value of stability margin. Voltage and stability margin regulation processes are connected to each other. Therefore they must be considered simultaneously. Furthermore, there is a need of identifying of voltage regulation influence on voltage stability margin. There will be considered three regulation possibilities: transformer tap changing, reactive power compensation and load shedding.

3.1. TRANSFORMER TAP CHANGING

Regulation of transformer tap should maintain voltage close to nominal according to power system configuration and node load changes. In situation when measured voltage is too high tap changer position should be decreased and when it is too low this position should be increased (Fig. 2). Those operations have impact on voltage stability margin what causes some limitations e.g. blocking of transformer tap changer [3, 4].

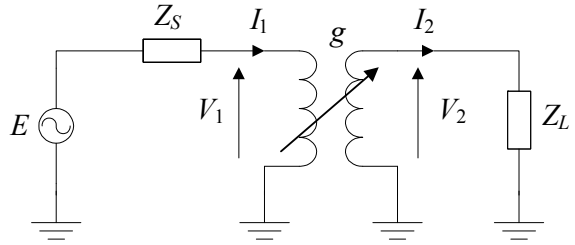

Fig. 2. Transformer with tap changer diagram

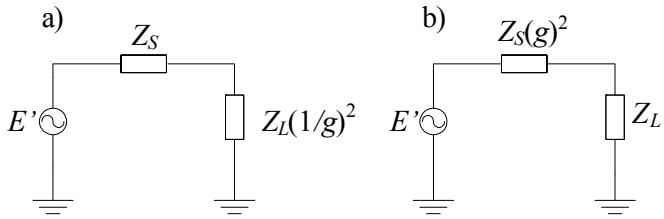

Fig. 3. Impedances calculated for each transformer windings

In Figures 3a and 3b there are presented impedances calculated to the primary and secondary winding of transformer. Voltage regulation (using tap changer), changes not only value of voltage but also stability margin of node. This is because when ratio g is bigger than nominal value g_n load impedance calculated to primary winding of transformer decreases. It causes decrease of stability margin:

$$\Delta W = 1 - \frac{|Z_S| g^2}{|Z_L|} = 1 - W g^2 \tag{8}$$

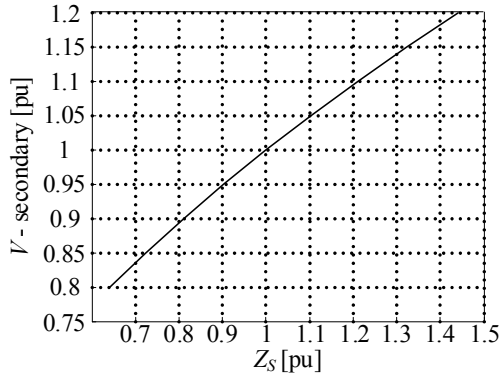

Fig. 4. The voltage and Z_S impedance of g ratio dependence

Figure 4 shows plot of the voltage against series impedance Z_S of g ratio dependence. The voltage at secondary winding of transformer depends on transform ratio g and series impedance Z_S depends on square of g ratio. Therefore, decrease of stability margin goes faster than the increase of value of voltage. As a consequence of increase of series system impedance stability margin $\Delta W = 1 - W$ decrease. That is why sometimes there is a necessity of blocking of transformer tap changer [3, 4].

3.2. REACTIVE POWER COMPENSATION

Other way of voltage control (that also causes decrease of power transmission losses) is compensation of reactive power in receiving node. Possible realization scheme is shown in Fig. 5. It can assumed that impedance Z_L has resistive-inductive character and source of capacitive reactive power is impedance Z_C. Vector plot corresponding to circuit from Fig. 5 is shown in Fig. 6. Figure 6a shows full compensation, 6b under compensation and 6c over compensation of reactive power. Compensation cause decreasing of the amplitude of current. In consequence equivalent load impedance increases and impedance angle decreases (to zero for full compensation), both of them cause increase of voltage.

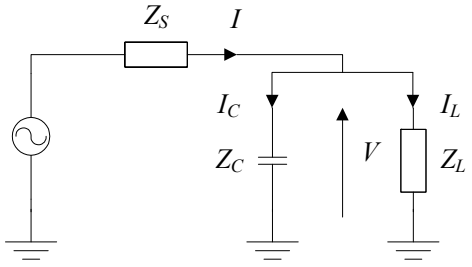

Fig. 5. Reactive power compensation scheme

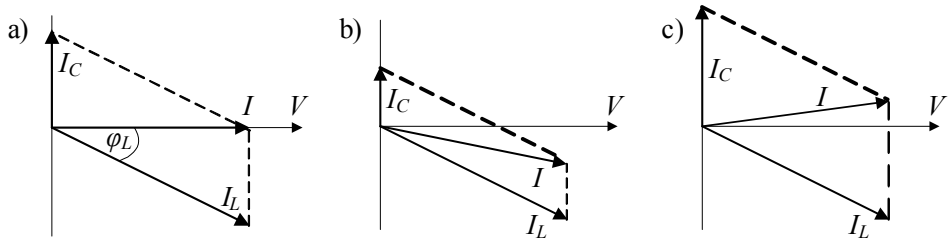

Fig. 6. Vector plot of reactive power compensation a) full compensation, b) under compensation, c)over compensation

Total impedance after compensation can be calculated from:

$$\overline{Z}_Z = \frac{\overline{Z_L} \cdot \overline{Z}_C}{\overline{Z_L} + \overline{Z}_C} = \frac{\left(R + j\omega L\right)\dfrac{1}{j\omega C}}{R + j\omega L + \dfrac{1}{j\omega C}} \tag{9}$$

$$\left|\overline{Z}_Z\right| = \frac{\left|Z_L\right|}{\sqrt{\left(1 - \omega RC \cdot \mathrm{tg}\,\varphi_L\right)^2 + \left(\omega RC\right)^2}} \tag{10}$$

$$\arg\left(\overline{Z}_Z\right) = \varphi_L - ar\,\mathrm{ctg}\left(\frac{\omega RC}{1 - \omega RC \cdot \mathrm{tg}\,\varphi_L}\right) \tag{11}$$

Denominator of equation (10) is less than one what ensures load impedance module increases and load angle decreases. It reduces power transmission losses and increases value of node voltage. From equation (10) condition of full compensation can be calculated. When full compensation occurs, argument of equivalent load impedance equals zero. After simple modifications the following condition is obtained:

$$\omega RC = \frac{tg\varphi_L}{1 + tg^2\varphi_L} \tag{12}$$

Equations (9, 10, 11) can be used to calculate required value of capacitance for given parameters of circuit. Instead of this there can be designed voltage regulation system. The system could keep value of voltage in specified range. Block diagram of concept of such system is shown in Figure 7. Regulation of Z_C impedance can be realized using power electronics.

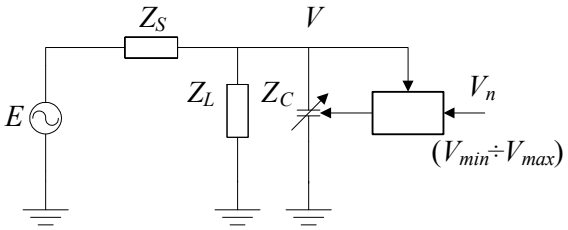

Fig. 7. Voltage regulation diagram

According to the diagram presented in Fig. 7 voltage control simulation tests were realized for two types of load: constant impedance and constant power [2]. Tests include monitoring of received power, voltage and stability margin changes. In simulation there were assumed constant angle of load ($\mathrm{tg}\varphi$ = 0.4) and load impedance decreased and increased two and three times. Plot 8 and 10 show changes of node

parameters without compensation for constant impedance and constant power models. As an effect of load impedance changes active and reactive power increased and voltage decreased. For constant power model changes have larger values than for constant impedance model.

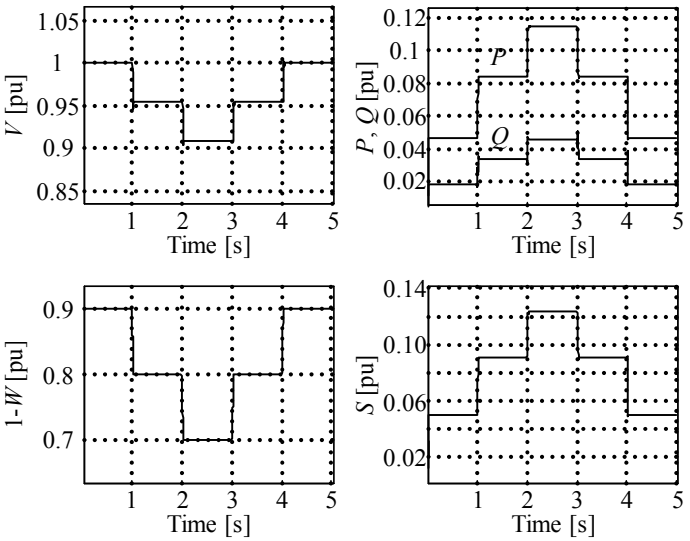

Fig. 8. Plots for constant impedance load model without compensation

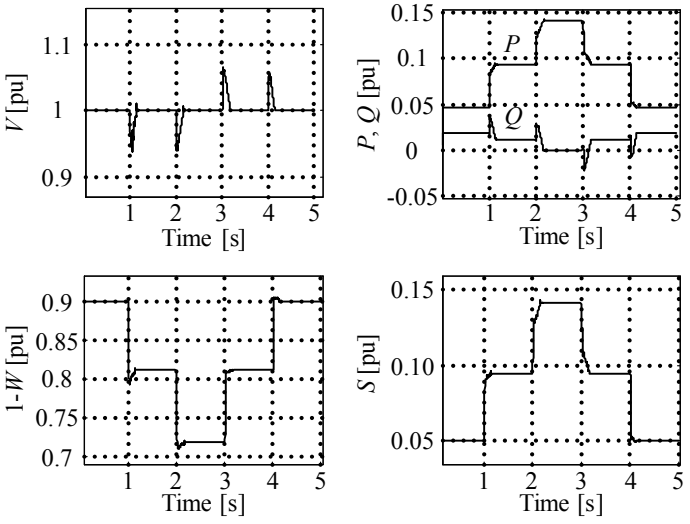

Fig. 9. Plots for constant impedance load model with compensation

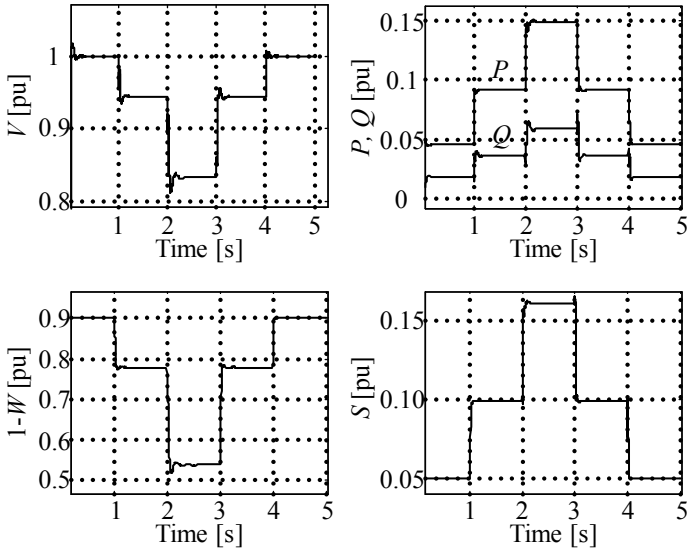

Fig. 10. Plots for constant power load model without compensation

When voltage of the node goes down the voltage control system starts its operation. Effect of this operation is reactive power decrease (compensation) and keeping node voltage at nominal level $V = 1$. Regulation of voltage also enlarges local stability margin. It is caused by changes of angle and module of equivalent load impedance.

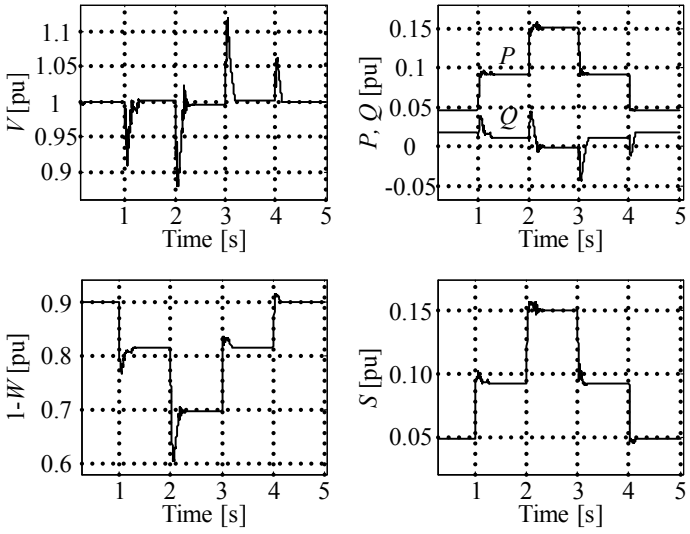

Fig. 11. Plots for constant power load model with compensation

3.3. UNDERVOLTAGE LOAD SHEDDING

In extreme case of voltage decrease (that cannot be regulated by tap changer and reactive power compensation undervoltage) load shedding can be rescued. Possibilities of the shedding are related to the social and business conditions but it is also important to study what effect will be achieved by disconnecting different types of loads. Two examples of the load shedding are shown in Figs. 12 and 13. In the first case (Figs. 12a, 13a) two constant impedances model with the same value but different angle are connected to the node. Plots 12a and 13a show result of disconnection one of them. Curve I presents exclusion of load with tgφ = 0.4 and curve II load with tgφ = 0. In the second set (Fig. 12b, 13b) there are two loads with the same value and angle but different types. One of them is constant power (III – disconnection of the model) and the second one constant impedance model (IV – disconnection of the model). Test consists three parts: 0-1s normal operation state, 1-2s state after doubling system impedance, 2–3s state after switching off one of two loads. Test with constant impedance models (Figs. 12a, 12b) shows that disconnection of one of them caused great voltage and small stability margin changes. In the second test (Figs. 12b, 13b) with mixed type of load it is important to decide which load should be disconnected. When constant power load is disconnected changes of voltage and stability margin are about two times larger than when constant impedance model is disconnected.

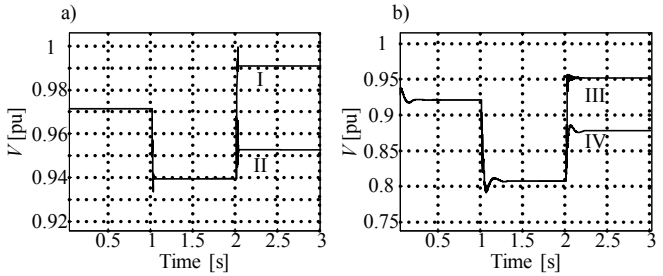

Fig. 12. Voltage plots of load shedding of constant impedance models (I – tgφ = 0.4, II – tg φ = 0) (a) and constant power – III and constant impedance – IV models (b)

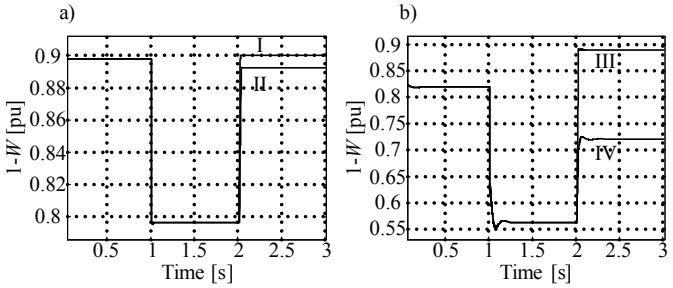

Fig. 13. Stability margin plots of load shedding of constant impedance models (I – tgφ = 0.4, II – tgφ = 0) (a) and constant power – III and constant impedance – IV models (b)

4. CONCLUSIONS

Local measurements obtained at receiving node of the power system can be used to control its voltage level and stability margin. This can be done by using Thevenin model. Also update of the model parameters can be made by using local measurements.

Simulation tests show that voltage regulation system by reactive power compensation has advantageous properties. It brings dual effect: voltage stabilisation and increase of local stability margin.

Illustrative examples show that algorithms of load shedding may be intelligently applied with load portioning to achieve the best possible stability and economic effects. Intelligent load shedding and voltage and stability margin control can be part of Smart Grid technology.

ACKNOWLEDGMENT

The paper was realized in framework N N511 472439 project sponsored by the Polish Ministry of Science and Higher Education.

REFERENCES

[1] BRUSIŁOWICZ B., REBIZANT W., SZAFRAN J., *A new method of voltage stability margin estimation based on local measurements*, APAP 2011 Conference, Beijing, No 1790, pp. 2443–2447.

[2] MACHOWSKI J., BIALEK W.J., BUMBY R.J., *Power system dynamics and stability*, John Wiley & Sons 1997.

[3] WISZNIEWSKI A., REBIZANT W., KLIMEK A., *Distributed stability control using intelligent voltage margin relay*, Proceedings of the CIGRE Canada Conference on Power System, Vancouver, paper 131, 17–19 October 2010.

[4] WISZNIEWSKI A., REBIZANT W., KLIMEK A., *Intelligent voltage difference control maintaining the voltage stability limit*, Proceedings of the 43th CIGRE Session, Paris, France, paper B5_107_2010 August 2010.

[5] VU K., BEGOVIC M.M., NOVOSEL D., SAHA M.M., *Use of local measurements to estimate voltage stability margin*, IEEE Transactions on Power System, Vol. 14, pp. 1029–1035, Aug. 1999.

CT saturation detection,
protective relaying,
transient analysis

Dominik BĄK*, Xinzhou DONG*,
Waldemar REBIZANT**

NEW METHOD OF CT SATURATION DETECTION

A new method for detection of CT saturation is presented in this paper. The presented algorithm applies a new, innovative methodology mapping first order derivative of phase current signals into coordinates of a 3D vector. The comparison of proposed algorithm with standard one based on secondary current signal's second derivative is conducted and some of simulation results are presented to show the proposed algorithm effectiveness.

1. INTRODUCTION

The inductive current transformers with solid iron ferromagnetic core (TPX) are nowadays still the most widely applied, in power systems, to provide the transformation of primary currents into secondary ones. They possess good transformation properties and guarantee high accuracy and reliability of secondary currents in most conditions. But even if selected properly according to [1] their magnetic cores can sometime experience saturation because of too large magnitude of a primary current or/and its exponential component. As CT saturation phenomenon can result in significant distorting of secondary current waveform, it may bring in serious inaccuracies into measurement results or decision-making procedures which may become unreliable or clearly wrong [13]. Thus power system reliability is jeopardised by maloperation of protection devices or/and controls.

The correct operation of protective relays depends on the quality of secondary current signals delivered into relay's inputs by current transformers. To guarantee it even in periods when the CT magnetic core gets saturated it is necessary to properly recognize

* State Key Laboratory on Power System, Department of Electrical Engineering, Tsinghua University, Beijing, China.
** Institute of Electrical Power Engineering, Wrocław University of Technology, Wrocław, Poland.

the beginnings and ends of deformations of a secondary current signal in order to block or rearrange the operation of automatic systems [7, 14]. It is also possible to undertake actions aiming at reconstructing the correct waveform of a secondary current.

The corrupted secondary current affects badly not only the work of on-line systems but can change results of fault location algorithms which run both in an on- or off-line manner as well [12].

The problem of a secondary current deformation because of CT saturation still is very important one to be solved. There are many reports available discussing this problem and proposing different way of dealing with it. [4, 7, 10, 14] cover the design of protection devices cooperating with CTs. Hardware oriented ones include [3]. A method dedicated to CT saturation detection and presented in [7] was assumed here as a reference one for testing the new proposed herein algorithm. One other report [5] recommends application of secondary current third derivative for that purpose. Among compensating algorithms for secondary currents [6] might also be mentioned. There are also reported other methods for detecting occurrence of current transformer saturation applying other approaches like artificial neural networks [11, 9] or wavelet transformation [8] for that purpose.

The new proposed in this paper method for detecting occurrences of current transformer saturation is developed within a project investigating a new method of secondary current waveform restoration. The paper is aimed at introducing new methodology basics and description of the algorithm for detecting periods of current transformer saturation. Results of current transformer saturation detection obtained in simulation tests of a current transformer modelled in ATP-EMTP are provided to show the effectiveness of the new proposed method.

2. METHODOLOGY FOR NEW ALGORITHM DESIGN

A phase current signal flowing in a power system lines can be described with general model as

$$i(n) = i_m \cos(\omega n T_s + \varphi) + \Sigma_h i_h(n) + \Sigma_T i_T(n) + d(n) \tag{1}$$

including beside the fundamental component fluctuating with rated frequency also higher harmonics, exponentially decaying with different time constants T components and other usually random disturbances. The actual content of current signal's components depends on the state of a power system and in case of higher harmonics it is limited by power quality standards as long a power system is in normal quasi steady state operation. During transients, especially following the inception of a fault, there appears an abnormal current with exponential components which together with augmented value of its fundamental component can originate a substantial enough shift of magnetic flux to make CT magnetic core saturate. In those conditions, the secondary

current waveform can suffer distortions which intensity reflects the degree (depth) of CT saturation. The fundamental component $i_{S1}(n)$ of it can be considered to be a superposition of the not deformed one and nonlinear component $i_N(t)$ equal to missing secondary current

$$i_{S1}(n) = (I_{Sm} + i_N(n))\cos(\omega n T_s + \varphi') \tag{2}$$

This decomposition of secondary current into symmetrical and asymmetrical parts allows for designing a very efficient algorithm for CT saturation detection within a framework of the new 3D methodology.

The key step of the method is that the samples of *ABC*-phase currents are considered to be the *xyz*-coordinates of a 3 dimensional Cartesian space vector called the line current vector as below

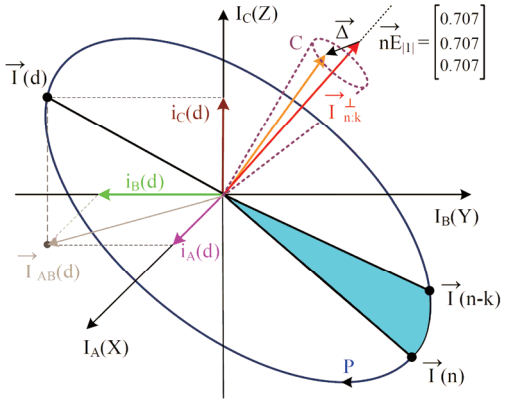

Fig. 1: Graphical presentation of relations between line current vector current perpendicular-to vector $\vec{I}_{n:k}^{\perp}$

$$\begin{cases} i_A(n) = X_{1m}\cos(\omega n T_s + \varphi_A) \\ i_B(n) = X_{1m}\cos(\omega n T_s + \varphi_B) \\ i_C(n) = X_{1m}\cos(\omega n T_s + \varphi_C) \end{cases} \rightarrow \vec{I}(n) = \begin{bmatrix} i_A(n) \\ i_B(n) \\ i_C(n) \end{bmatrix} \tag{3}$$

which rotates around the space centre scratching a closed curve corresponding to a given steady state of power system operation, see Fig. 1.

Shifting the analysis of power system phenomena from a two dimensional impedance plane to a three dimensional space shows them in a new perspective and these newly observed features can be successfully applied for a power system protection purposes.

Different steady state conditions of power system operation are now mapped into closed curves in a three dimensional space. Curves are housed in planes distinguished

by a current perpendicular-to vector calculated as a vector product of a actual and delayed by k samples line current vectors as follows

$$\vec{I}^{\perp}_{n:k} = \vec{I}(n) \times \vec{I}(n-k) = \begin{bmatrix} \vec{I}^{\perp}_{n:k}(x) \\ \vec{I}^{\perp}_{n:k}(y) \\ \vec{I}^{\perp}_{n:k}(z) \end{bmatrix} = \begin{bmatrix} \left(i_B(n)i_C(n-k) - i_C(n)i_B(n-k)\right)_x \\ \left(i_C(n)i_A(n-k) - i_A(n)i_C(n-k)\right)_y \\ \left(i_A(n)i_B(n-k) - i_B(n)i_A(n-k)\right)_z \end{bmatrix} \tag{4}$$

Compared to the line current vector (3) the current perpendicular-to vector (4) is almost steady in space. It can be shown that all normal states of power system operation can be described with current perpendicular-to vectors of different length but all of which have the same spatial orientation with reference to *xyz*-axis.

During transients current perpendicular-to vector moves from its normal position to a new one characteristic for a given disturbance and stays there as long as the disturbance lasts.

As each different state of power system can be now associated with a unique position of a current perpendicular-to vector then any deviations from them are referred to various additional abnormal conditions occurring in power system operation and are subjected to protective relaying. The investigation of those deviations allows for identifying the ones corresponding to current transformer saturation and to develop an algorithm responsible for detecting and indicating those conditions.

3. CRITERION QUANTITY SIGNAL

The criterion quantity signal used for detecting occurrences of CT saturation is a measure of spatial orientation deviations of the current perpendicular-to vector (4), which are substantial while CT saturation starts and ends, as presented in Figure 2b. Observed damped oscillations of the current perpendicular-to vector coordinates are driven by exponential components present in phase-to-phase fault current signals, see Figure 2a.

Calculating the first order derivative of current perpendicular-to vector coordinates a vector signal is obtained:

$$\Delta_d \vec{I}^{\perp}_{n:k} = \vec{I}^{\perp}_{n:k} - \vec{I}^{\perp}_{n-d:k} \approx f_t'(i_N(n)) \tag{5}$$

It carries on the information focused on changes of phase current signal disturbances in time, among which the nonlinear current component $i_N(t)$ introduced in (2) is the largest component.

As the computation process of a current perpendicular-to vector mixes the information on two different phase currents together it incorporates a natural redundancy of them into each one vector's coordinate. To bring it out a vector

$$\Delta^{\downarrow}\vec{I}^{\perp}_{n:k} = \begin{bmatrix} \vec{I}^{\perp}_{n:k}(y) - \vec{I}^{\perp}_{n:k}(z) \\ \vec{I}^{\perp}_{n:k}(z) - \vec{I}^{\perp}_{n:k}(x) \\ \vec{I}^{\perp}_{n:k}(x) - \vec{I}^{\perp}_{n:k}(y) \end{bmatrix} \approx f_t'(i_N(n)) \tag{6}$$

called a current perpendicular-to detail vector is obtained. It also carries the information focused on phase current signals' disturbances and like (5) is a function of the nonlinear current component $i_N(t)$ introduced in (2). Comparing the formulas (5) and (6) the current perpendicular-to detail vector (6) can be considered as a spatial derivative of a current perpendicular-to vector (4).

Combining together equations (5) and (6) a criterion quantity

$$C_{3D}(n) = \Delta_d \vec{I}^{\perp}_{n:k}(z) - \Delta d\vec{I}^{\perp}_{n:k}(y) \tag{7}$$

for detecting CT saturation is created. Criterion quantity signal vector's coordinates are shown in Figure 2c. Identifying high peaks and low lows allows for detecting when CT saturation starts and ends.

4. CT SATURATION DETECTION TECHNIQUE

The design of decision-making procedure for CT saturation detection depends on how signals being components of a criterion quantity vector (7) are computed. There are two possible ways.

The first one was presented in paragraph 3. It is easy but requires complicated decision-making system analysing all three components of a criterion quantity vector (7) simultaneously. It is not to be discussed in this paper.

The other one based on the slightly modified concept of the first one and allows for considering only one coordinate of (7). In this case one criterion quantity vector with three meaningful coordinates is replaced with three criterion quantity vectors with only one meaningful coordinate. These three individual criterion quantity vectors are defined each one for different phase current signal accompanied with two virtual sine waves in place of other two real phase signals. Such a rearrangement results in a very simple decision-making scheme which additionally is almost the same as the one applied for a reference method [7]:

$$C_{3D}(n) \geq TS(n) \;\&\; CT_{SAT} = NO \rightarrow CT_{SAT} := YES \tag{8}$$

$$C_{3D}(n) \geq TN(n) \;\&\; CT_{SAT} = YES \rightarrow CT_{SAT} := NO \tag{9}$$

if only self-adapting thresholds $TS(n)$ and $TN(n)$ in (8), (9) are kept constant.

5. SIMULATION RESULTS

Simulation research of detecting distorted, due to CT saturation, secondary current signals was performed using CT model described in [2] and proved correct operation of proposed algorithm. The proposed algorithm correctly recognised and marked periods of secondary current collapse caused by occurrence of CT saturation phenomenon.

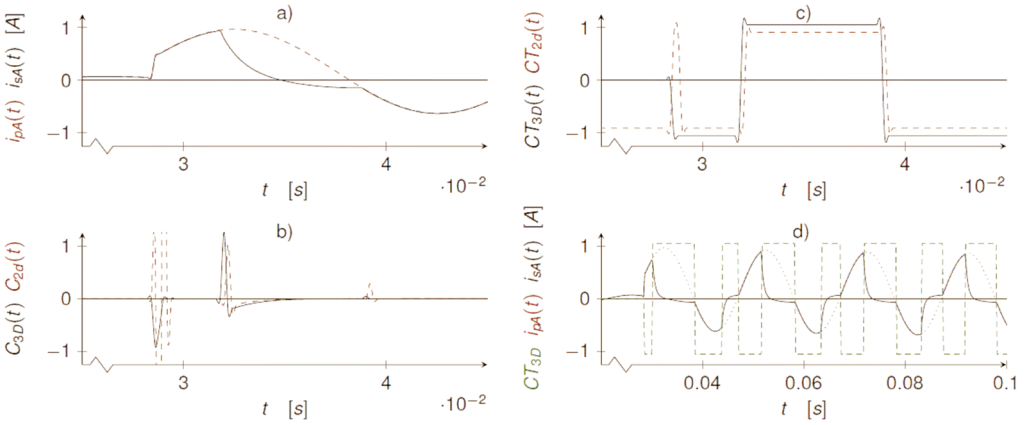

Fig. 2. Single phase fault: a) primary and secondary current signals;
b) comparison of criterion signals;
c) comparison of CT detection, d) Example of CT saturation detection:
CT alarm, primary and secondary current signals

A designed criterion quantity signal's shape which is similar to the one obtained by calculating a reference measure [7], makes it possible to apply the same decision-making procedure and allowing for reliable comparing of the results obtained by both proposed and reference algorithms. Shapes of both criterion quantity signals received in case of a phase-to-ground fault, presented in Fig. 2a, are pictured in Fig. 2b. Both algorithms detected occurrences of CT saturation in a faulty phase current as shown in Figure 2c. The proposed 3D algorithm identifies the inception and final moments of CT saturation faster – without any delay – as this algorithm employs only computing of first order derivatives of current signals for the actual signal sample while the reference algorithm applying the second order derivative calculated with five-point formula lags by two sampling periods. Figure 2d demonstrates another results of CT saturation detection achieved with the new proposed 3D method. It can be seen that all occurrences of CT saturations were correctly detected and signalled out.

6. CONCLUSIONS

A new algorithm for detecting CT saturation was presented in the paper. Simulation research confirmed high effectiveness of detecting distorted parts of secondary current signals by the new algorithm which identified them correctly and without any additional delay.

As the proposed algorithm is also based on signal's derivative calculation which results in its high sensitivity to any noises. It was found out that the decisive part of the algorithm should be reconsidered in dependence to applied model or real magnetising characteristic of a given current transformer type. Therefore further research is needed to improve the decision-making part of the algorithm by introducing some self-adapting properties to make it independent of magnetising characteristic modelling manner.

ACKNOWLEDGEMENTS

The paper was written within a NSFC Major International Cooperation Project No. 51120175001 and NFSC Key Project No. 50377019.

REFERENCES

[1] ANSI/IEEE C37.110 Standard: IEEE Guide for the application of current transformers used for protective relaying purposes.

[2] BĄK D.J., DONG X.Z., WANG B., SHI S.X., REBIZANT W., *New Method of Detection of Current Transformer Saturation*, [in:] Proc. of the DPSP2012 Conference, Birmingham, United Kingdom, 2012, paper 0168.

[3] BRADLEY D.A., GRAY C.B., KELLY D.O., *Transient compensation of current transformers*, IEEE Trans on PAS 97(4), 1978, 1264–1271.

[4] BUNYAGUL T., CROSSLEY P.A., *Design and evaluation of an overcurrent relay suitable for operation with measurement current transformers*, [in:] Proc of 7th Int Conf on Developments in Power System Protection – DPSP, IEE CP479, 2001, 201–204.

[5] KANG Y., KANG S., CROSSLEY P.A., *An algorithm for detecting CT saturation using the secondary current third-derivative function*, [in:] Proc. of the IEEE Bologna PowerTech Conference, Bologna, Italy, 2003, 320–326.

[6] KANG Y.-C., KANG S.-H., PARK J.-K. et al., *Development and hardware implementation of a compensating algorithm for the secondary current of current transformers*, IEE Proc – Electr. Power Appl., 43(1), 1996, 41–49.

[7] KASZTENNY B., ROSOŁOWSKI E., ŁUKOWICZ M., IŻYKOWSKI J., *Current related relaying algorithms immune to saturation of current transformers*, [in:] Proc. of 6th Int. Conf. on Developments in Power System Protection DPSP, IEE CP434, 1997, 365–369.

[8] LI F., LI Y., AGGARWAL R.K., *Combined wavelet transform and regression technique for secondary current compensation of current transformers*, IEE Proc. – Gener. Transm. Distrib. 149(4), 2002, 497–503.

[9] REBIZANT W., BEJMERT D., *Current transformer detection with genetically optimized neural networks*, Proc. of the 2005 IEEE PowerTech Conference, St. Petersburg, Russia, CD-ROM, paper 220, June 2005.

[10] REBIZANT W., HAYDER T., SCHIEL L., *Prediction of CT saturation period for differential relay adaptation purposes*, [in:] Proc. of the 14th Power System Protection Conference PSP ’04, 2004, 24–129.
[11] SAHA M., IŻYKOWSKI J., ŁUKOWICZ M., ROSOŁOWSKI E., *Application of ANN methods for instrument transformer correction in transmission line protection*, [in:] Proc. of the 7th Conf. on Developments in Power System Protection, Amsterdam, the Netherlands, April 2001, 303–306.
[12] SAHA M., IŻYKOWSKI J., ROSOŁOWSKI E., *Fault location on power networks*, Springer, London, 2010.
[13] WISZNIEWSKI A., *Fault location correction of errors due to current transformers*, [in:] Proc. of 3rd Int. Conf. on Developments in Power System Protection – DPSP, CP249, 1985, 185–187.
[14] WISZNIEWSKI A., SZAFRAN J., *Distance algorithm immune to saturation of current transformers*, [in:] Proc. of 4th Int. Conf. on Developments in Power System Protection – DPSP, London, IEE CP302, 1989, 196–199.

dynamic thermal line rating,
distance protection, overload, heat balance

Łukasz STASZEWSKI*
Waldemar REBIZANT*

DISTANCE PROTECTION WITH DYNAMIC THERMAL LINE RATING ENHANCEMENT

As the worldwide analysis of recent wide area cascading failures have shown, very often the main cause of blackout was mal-operation of the third zone of a distance protection relay. The load encroachment and power swing phenomena are the two dire problems to solve when dealing with the third zone of distance protection mal-function. The vast number of blackouts could have been avoided or the consequences lowered if the distance relay had not operated due to controlled impedance encroachment.

This paper proposes a new approach to enhance the distance protection relay operation by introducing a new blocking algorithm. The algorithm is based on Dynamic Thermal Line Rating (DTLR) idea to restrain relay from tripping when conditions in electrical power system and weather conditions allow for it.

1. PRINCIPLES OF DISTANCE PROTECTION

The basic principle of distance protection involves the division of the voltage at the relaying point ($\overline{V}_R$) and the measured current ($\bar{I}_R$) phasors as it can be seen in (1). The apparent impedance calculated in this way is compared with the reach point impedance/characteristic.

$$\overline{Z}_R = \frac{\overline{V}_R}{\bar{I}_R} \tag{1}$$

If the measured impedance is lower than the relay reach, it is concluded that a fault exists on the line at a place between the relay and the reach point.

* Wrocław University of Technology, Institute of Electrical Power Engineering, Wybrzeże Wyspiańskiego 27, 50-370 Wrocław, Poland.

A distance relay is designed to operate only for faults occurring between the relay location and the selected reach point, thus giving discrimination for faults that may occur in different line sections and making protection selectivity assured.

The reach point of a relay is the point along the line impedance that is intersected by the boundary characteristic of the relay. Since this is dependent on the ratio of voltage and current and the phase angle between them, it may be plotted on an R/X diagram as in Fig. 1. The loci of power system impedances as seen by the relay during faults, power swings and load variations may be plotted on the same diagram and in this manner the performance of the relay in the presence of system faults and other disturbances may be studied. This fact will be taken into account in this paper for zone 3 distance relay impedance characteristic encroachment to show the situations of power swing and load increase during particular system conditions and their influence on the distance relay operation.

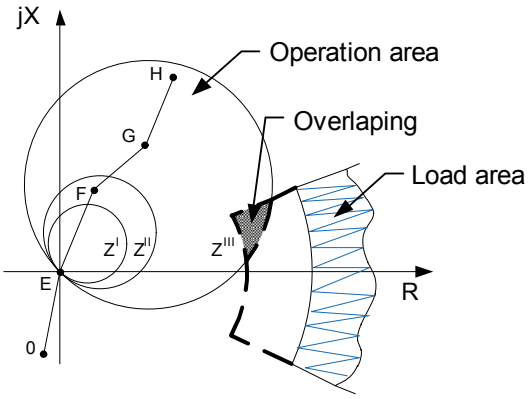

Fig. 1. Distance relay characteristic of operation for Zone 1, Zone 2 and Zone 3

Careful selection of the reach settings and tripping times for the various zones of protection enables correct co-ordination of the distance relays on a power system. Main distance protection will comprise instantaneous directional Zone 1 and one or more time-delayed zones. Typical settings for three forward zones of basic distance protection are given as follows. Zone 1 settings of up to 85% of the protected line impedance. The resulting 15–20% safety margin ensures that there is no risk of the Zone 1 protection over-reaching due to errors in the current and voltage transformers, inaccuracies in line impedance data provided for setting purposes and errors of relay setting and measurement. Otherwise, there would be a loss of discrimination with fast operating protection on the following line section. Zone 2 of the distance protection must cover the remaining 15–20% of the line plus apart of following line section [5].

To ensure full coverage of the line with allowance for the sources of error already listed above, the reach setting of the Zone 2 protection should be at least 120% of the

protected line impedance. In many applications it is common practice to set the Zone 2 reach to be equal to the protected line section +50% of the shortest adjacent line.

Remote back-up protection for all faults on adjacent lines can be provided by a third zone of protection that is time delayed to discriminate with Zone 2 protection plus circuit breaker trip time for the adjacent line. Zone 3 reach should be set to at least 1.2 times the impedance presented to the relay for a fault at the remote end of the second line section.

On interconnected power systems, the effect of fault current infeed at the remote busbars will cause the impedance seen by the relay to be much greater than the actual impedance to the fault and this needs to be taken into account when setting Zone 3. As the third zone of impedance relays with mho-characteristic covers significant part of the system and thus the impedance characteristic area is big, it is mostly vulnerable to abnormal conditions in the electrical power system operation.

The third zone is especially exposed to load encroachment, power swing and voltage instability – all three situations can lead to measured impedance entering into the Zone 3 characteristic what results in relay mal-operation and can be a leading factor causing a large scale blackouts, as it could be seen, e.g., in Germany on November 4th in 2006 [6].

Despite the fact of Zone 3 setting encroachment, the system operational situation may not be dangerous and in case of load encroachment the load may be permissible due to the transmission lines loadability, and in case of power swing, after some time the system recovers to its normal operation not causing any danger during the restoration time. The important issue is to distinguish whether the encroachment is a result of fault and the relay should operate, or it is one from above-mentioned situations and the relay tripping decision should be restrained.

2. DYNAMIC THERMAL LINE RATING FOR LOAD ENCHROACHMENT

There are many various ways to avoid over-tripping due to unwanted impedance encroachment, both at the level of protection designing (characteristic shape shifting, adding restrictions) and during the relay operation (measuring additional criteria signals, e.g., zero sequence current). However, it is very difficult to predict all possible situations in a given system and all possible operation conditions, thus none of them is perfect. This paper is focused on the possibility of DTLR usage to prevent distance protection relay from tripping in situations of extreme load conditions and power swing by introducing an additional blocking signal into the standard distance relay. The blocking signal is based on the DTLR technique measuring weather conditions and calculating the overhead conductor temperature and actual conditions conductor current limit as well as the time left to reach the thermal limit.

The DTLR application aims at real time calculation of an overhead bare conductor ampacity dependent on the ambient weather conditions. The DTLR algorithm cooperates with standard protection devices (MHO distance protection relay) in order to fully utilize the transmission line by calculation of temporary current-carrying capability. The conductor temperature is calculated from the standard heat balance equation, according to the IEEE standard [3]:

$$q_c + q_r = q_s + q_i \tag{2}$$

where: q_c is a heat dissipation due to convection, q_r due to radiation, and q_s and q_r are heat gain due to solar radiation and due to Joule's law caused by the current flow, respectively. Considering the part of the total amount of heat gain and dissipation the biggest is Joule's heating and wind-forced convection cooling, the lesser are solar heat and radiated cooling.

Starting from Equations (2) and considering the conductor temperature change in time it is possible, using numerical solution, to calculate the current conductor temperature from the Equation (3) as well as the time needed for the conductor to reach its thermal limit – according to the actual current value and weather conditions:

$$\frac{dT_C}{dt} = \frac{1}{mC_p}[R(T_C)I^2 + q_s - q_c - q_r \tag{3}$$

where: T_C is conductor temperature, m is mass of conductor and C_p is specific heat of conductor material, R is conductor resistance dependent on the conductor temperature and I is the magnitude of current flowing through the conductor.

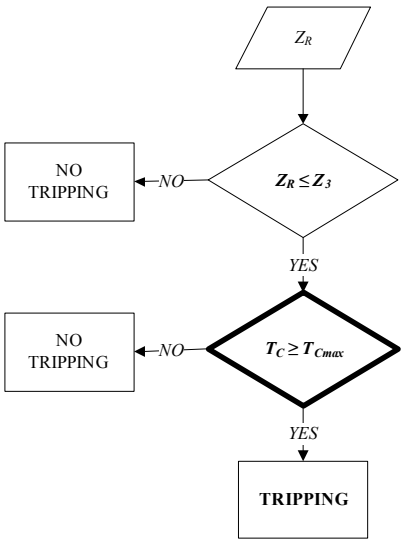

Fig. 2. Scheme diagram of a distance protection relay with additional DTLR support

Using the Dynamic Thermal Line Rating enhancement creates a possibility of reliability improvement of a standard distance protection relay in both load encroachment and power swing occurrences. The DTLR application introduces into a standard distance relay an additional algorithm, based on real time conductor temperature calculation, with the aim of blocking the tripping decision for some permissible time. Using Equation (3) computing there is a possibility to calculate that time and adjust the relay setting only for it. The scheme diagram of DTLR supported distance relay protection operation is presented in Fig. 2 with the new decision-restraining part. When the impedance seen by the relay encroaches the third zone of protection the restraining algorithm compares the current conductor temperature with the conductor's thermal limit and then restrain or not the tripping-decision.

For the measurement of criteria signal of distance protection used in this study full-cycle fast Fourier transformation was applied [4].

Considering the problem of backing up the line protection from the distance relay located at one side of a multi-line terminal it must be taken into account the third zone setting would be much greater than in two-line terminal. For system arrangement as shown in Fig. 3, it is as follows:

$$Z_3 = Z_{AC} + 1.2Z_{CP}\left(1 + \frac{I_{BC} + I_{MC} + I_{NC}}{I_{AC}}\right) \tag{4}$$

whereas in an extreme situation of equal contribution to the fault currents from all the lines the setting would be:

$$Z_3 = Z_{AC} + 4.8Z_{CP} \tag{5}$$

This makes the third zone much bigger. For the study, taking into consideration the further case of 250 km AFL 6 240 lines each, the Z_3 impedance settings for two-line terminal ($Z_{3(2)}$) and for multi-line one ($Z_{3(multi)}$) would be, respectively:

$$\begin{aligned} Z_{3(2)} &= Z_{AC} + 1.2Z_{CP} = 235.752\,\Omega \\ Z_{3(multi)} &= Z_{AC} + 4.8Z_{CP} = 621.516\,\Omega \end{aligned} \tag{6}$$

The multi-line substation for influence analysis of system topography on the third zone of impedance protection is illustrated below:

The described earlier issue has significant influence on both the system reliability and loadability. Increased zone 3 reach causes the distance relay characteristic approaching to the normal load impedance area, making possible the heavy load impedance to encroach it (Fig. 4).

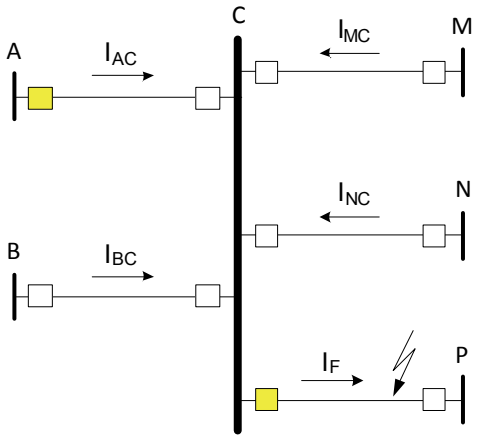

Fig. 3. Multi-line terminal (substation)

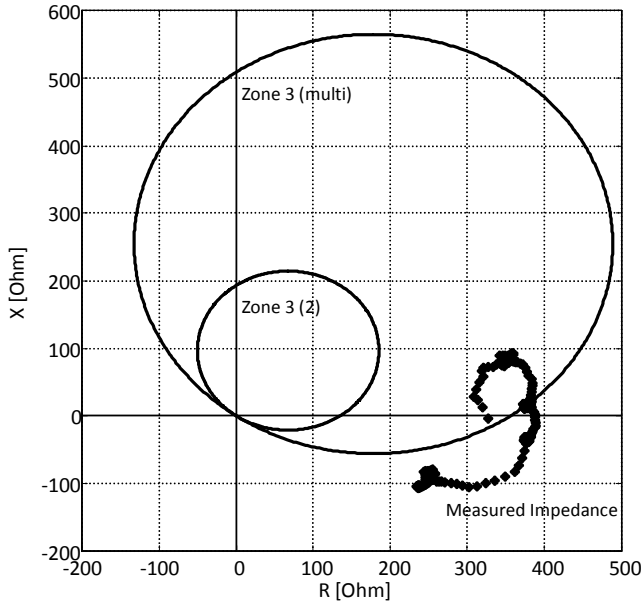

Fig. 4. Zone 3 settings for multiline and 2 lines terminal

Allowance of the heavy load impedance to encroaching third zone and not restraining the tripping decision causes using the transmission lines not fully. The load limit lowered in comparison to the actual lines capability and also – which seems to be more dangerous – creates a possibility for the distance relay to trip the heavily loaded transmission line. This may lead to the cascading event development and maybe even

lead to a blackout. This issue has been solved with use of DTLR algorithm application and the results of investigation are presented below.

The Dynamic Thermal Line Rating can be used for transmission optimization by temporary increasing current carrying capacity of transmission lines according to the weather conditions. This issue was also taken into account during the studies and therefore the simulation cases considered only the situations with both increase of load over the nominal rated level for transmission line overhead conductors and load encroachment of the third zone of the distance protection relay caused by the current increase [2].

For the sake of simulation the AFL 6 240 conductor was taken, at 110 kV transmission overhead line. The AFL 6 240 conductor ratings are 645 A and 745 A, respectively for summer and winter, with 60 Celsius deg. of maximum allowable conductor temperature. The investigation on the load encroachment was carried out using simulation in MATLAB Simulink in a system configuration shown in Figure 3. The load changes in transmission line were simulated as follows: increase in transmission line during the summer time from about 606 A to approximately 755 A at 50th minute of simulation time, thus exceeding its summer rating by 110 A (17%) and causing the load encroachment as in Fig. 4. The total time of simulation was 120 minutes.

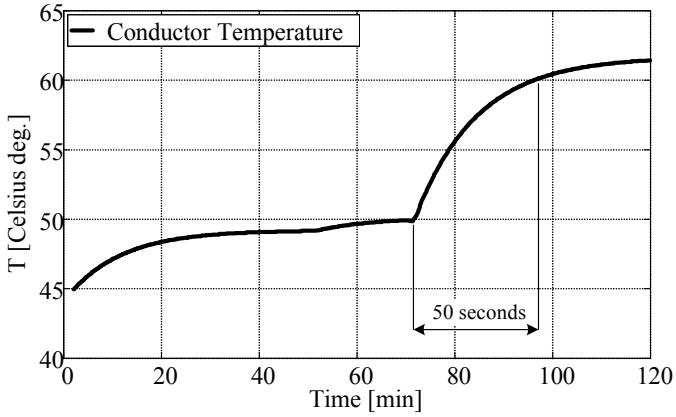

Fig. 6. Overhead transmission line conductor temperature during moderately favourable weather conditions

In the first example, assuming moderately favourable weather conditions, the temporary conductor current rating was set to 748 A (for the 30 Celsius deg. ambient air temperature, 4.5 m/s wind speed and high solar radiation). As it can be seen in Fig. 6, the DTLR algorithm was able to handle the current increase, therefore lengthening the transmission operation time for over 25 minutes and restraining the distance protection relay from tripping the line, while still safely operated.

Despite the fact that after those 25 minutes the relay will still operate tripping the line, the DTLR algorithm can give the information to the system operator about the remaining time, thus allowing him/her to make appropriate decision about adapting the system configuration to the currents needs (e.g., turning off less important consumers).

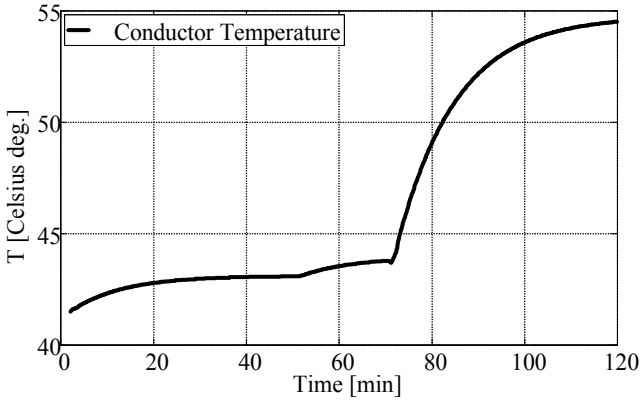

Fig. 7. Overhead transmission line conductor temperature during very favourable weather conditions

The second example, presented in Fig. 7, is based on the same values of current, still with load encroachment occurring but with more favourable weather conditions than in the first case (for the 25 Celsius deg. ambient air temperature, 6.0 m/s wind speed and moderate solar radiation) with temporary rated current value of 791.5342A, thus allowing the transmission line to be operated continuously with the given high load. This is possible since for the given weather conditions and current values the conductor will never be able to reach its thermal limit of 60 Celsius deg.

Both described above situations show that the use of Dynamic Thermal Line Rating application makes possible the power system protection reliability and transmission efficiency to increase.

3. DYNAMIC THERMAL LINE RATING FOR POWER SWING

This section presents the DTLR application and impedance relay performance in case of a power swing. The power swing phenomenon occurs, in presented in Fig. 8 system, due to transmission line disconnection during the process of a fault clearance.

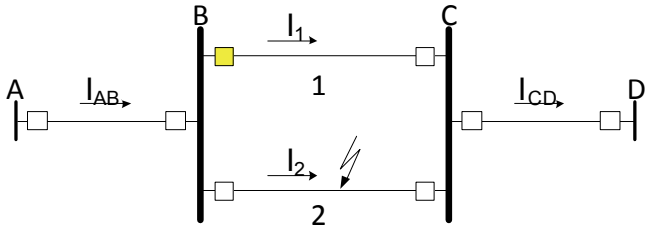

Fig. 8. Power system configuration for power swing investigation

In a result of fault on line 2 the circuit breakers at both its ends operated and the relay impedance transients measurements occurred to be as seen in Figure 9 below:

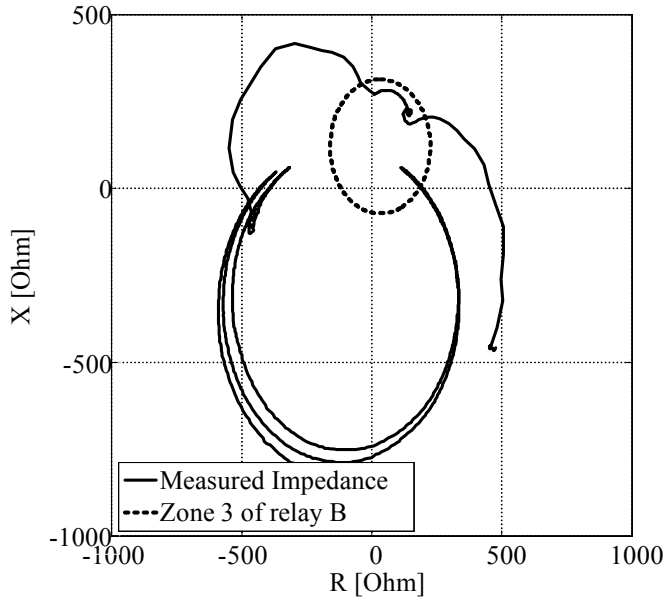

Fig. 9. Impedance during the power swing measured by the distance relay

For the impedance trajectory as above, the standard distance relay without additional blocking would operate, tripping the line 1 and causing loss of power transmission in this area. However, application of the Dynamic Thermal Line Rating highly improves the system reliability also in this situation.

It is worth mentioning at this point that only three phase faults were considered here, because other faults can be easily distinguished from the load changes by the zero sequence presence in current and voltage signals. Thus in case of three phase faults the current ratio is very high in comparison to the normal load conditions

(40 times higher or more) thus results in high value of a temperature change ratio per considered unit of time:

$$\frac{dT_C}{dt} \geq limit \tag{7}$$

where T_C is a conductor temperature, *dt* represents the temperature sampling time and *limit* stands for the value of change rate, which is different for every conductor, and its specific value will not be considered here.

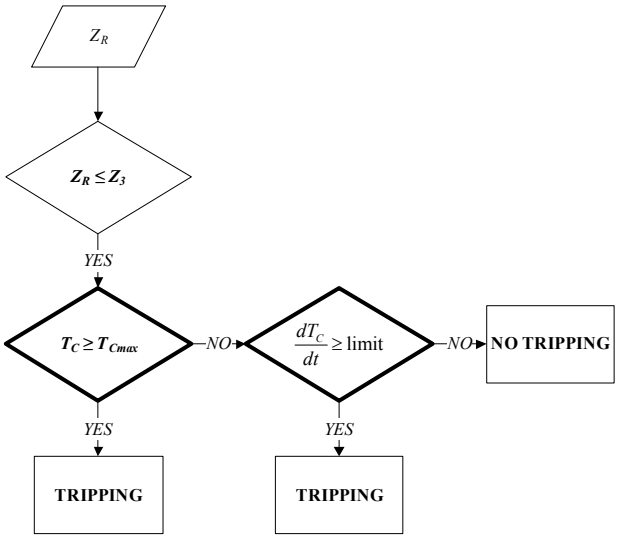

Fig. 10. Scheme diagram of improved algorithm of a distance protection relay

Power swing problem is more complex than the previous one, and requires additional part of algorithm (Fig. 10) for the derivative calculation. First of all, combining the two facts of impedance encroachment and current values higher than the summer rating leaves no doubts that the standard relay would operate.

The standard time delay of the 3rd zone for the sake of protection selectivity is 90 cycles (50 Hz – 1.8 seconds). In this case the additional algorithm which is based on a conductor temperature derivative was introduced. It can clearly distinguish the fault conditions from the load increase because of the rate of change in current values. It is well known that this value is totally different for power swing (rather low), and fault occurrence situations (rather high).

The DTLR algorithm, based on the conductor temperature calculation and the rate of its change is a way to avoid the relay operation what enables operating power system stably and safely despite of the transient situation. Figure 11 presents the thermal behaviour of the transmission line conductor during the favourable weather conditions.

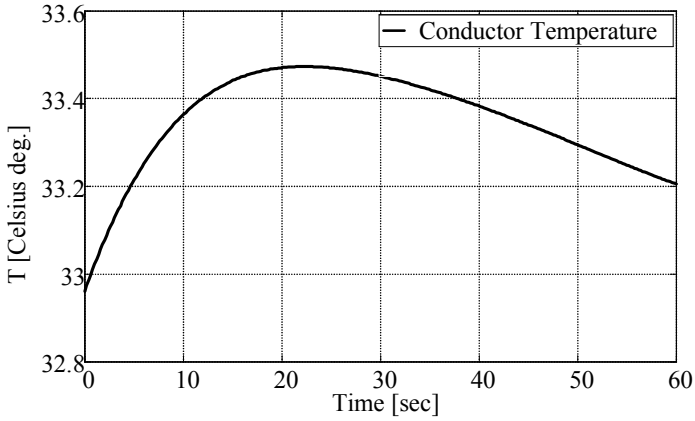

Fig. 11. Conductor temperature during power swing

Because of the thermal time constant of a conductor, which is about 15 minutes, for the met conditions the conductor temperature does not change significantly, which results also in a low value of derivative from Equation (7). Thus, due to the favourable weather condition, the conductor does not exceed its thermal limit and because of the low temperature change ratio the presented DTLR algorithm allows safe operation.

4. CONCLUSIONS

The Dynamic Thermal Line Rating application may seem to be very good in performance, however not always. It is highly dependent on the weather conditions. When they are favourable the DTLR can perform very well and can introduce much better transmission line utilization and transmission system efficiency. It can also improve the system reliability and safety, and can sometimes act as an anti-blackout protection, avoiding unnecessary relay operation. Introduction of two additional parts of DTLR algorithm into the standard distance protection relay resulted in better performance and reliability of the relay which makes it worth considering for future transmission installation or upgrade of existing electrical power systems.

REFERENCES

[1] DOUGLASS D.A.,. EDRIS A.-A., *Field Studies of Dynamic Thermal Rating Methods For Overhead Line*, Transmission and Distribution Conference, IEEE, Vol. 2, 1999, pp. 842–851.

[2] HOROWITZ S.H., PHADKE A.G., *Third zone revisited*, IEEE Transactions on power delivery, Vol. 21, January 2006, pp. 23–29.

[3] *IEEE Standard for Calculating the Current-Temperature of Bare Overhead Conductors*, IEEE Std 738-2006 (Revision of IEEE Std 738-1993).

[4] REBIZANT W., SZAFRAN J., WISZNIEWSKI A., *Digital Signal Processing in Power System Protection and Control*, Springer Verlag, Series: Signals and Communication Technology, London, 2011.
[6] WISZNIEWSKI A., UNGRAD H., WINKLER W., *Protection techniques in electrical energy systems*, New York, 1995.
[4] YAMASHITA K., LI J., ZHANG P., LIU C.-C., *Analysis and Control of Major Blackout Events*, IEEE, 2009.

grid-connected PV power plant,
transient analysis, fault contribution,
overcurrent protection

Daniel BEJMERT*
Tarlochan S. SIDHU**

SHORT-CIRCUIT CURRENT CONTRIBUTION FROM LARGE SCALE PV POWER PLANT IN THE CONTEXT OF DISTRIBUTION POWER SYSTEM PROTECTION

The interconnection of distributed generators (DG) to existing network may give rise to many technical problems. To ensure appropriate power quality and stability of the grid these problems should be recognized and solved. For this purpose, behaviour of such energy sources, under various disturbances, must be studied and known to the distribution grid operators. In this paper fault current contribution from large scale photovoltaic (PV) power plant as well as protection issues concerning such DGs are discussed. The mentioned problems were investigated in PSCAD model of 50 MW grid-connected PV power plant where various operating condition of the network and penetration levels of PV were considered.

1. INTRODUCTION

Due to growing requirements related to environmental and economic objectives imposed on energy sector, cause that renewable energy sources are more and more frequently employed. Solar energy belongs to one of the important and very resiliently developing sources of non-polluting energy. Significant increase of photovoltaic industry is observed not only in small scale systems (power range of kilowatts) but also in large scale ground-based arrays of tens of MW. Since the number of large scale photovoltaic systems has increased in the past several years many issues related to integration of this sources of energy into power system need to be discussed. There are many papers and reports that analyse the following aspects [5, 6, 8–10]:

* Institute of Electrical Power Engineering, Wrocław University of Technology, Wrocław Poland.
** University of Ontario Institute of Technology, Faculty of Engineering and Applied Science, Canada.

- design, construction and operation of PV systems;
- environmental and economic analysis;
- interaction with distribution network,
- operation of PV array (I-V and P-V characteristics) under variable weather conditions;
- enhancement of controllers' performance;
- anti-islanding protection;
- reduction of harmonic distortion;
- energy storage systems.

However, from the viewpoint of both power protection vendors and power system utilities, another issue should be analyzed as well. Since a large scale PV power plant of dozens of MW may be a significant source of short-circuit current, therefore, the following question arises: whether influence of such power source should be taken into consideration when protective system performance is analyzed. Because the fault contribution from PV power plant is limited by the maximum current level of the applied inverters, it may seem that the short-circuit current of the PV modules may have insignificant impact on MV protections [1, 4, 11]. Nevertheless, various issues of protection operation due to grid-connected PV systems are still reported [2]. Furthermore, in case of large scale photovoltaic power generation (in the above referred papers, only small scale PV systems have been considered) when PV system power is substantial, short-circuit current contribution from PV may lead to false relaying operation despite above mentioned limiting of the inverter current. Thus, such problem should be thoroughly investigated.

In this paper, short-circuit current contribution from large scale PV power plant in the context of distribution power system protection performance is discussed. In order to investigate the problem, appropriate power system model of a real distribution network has been prepared with the use of PSCAD simulation tool. Using the prepared model, a wide range of fault disturbances that may occur in a distribution network have been simulated. Finally, the most interesting cases are presented in the paper, conclusions are drawn and appropriate recommendations are made.

2. SIMULATION MODEL OF THE GRID-CONNECTED PHOTOVOLTAIC POWER PLANT

In this section a PSCAD model of a typical distribution network with interconnected PV power plant is presented. The following subsections contain comprehensive model description of: solar cell, maximum power point tracking controller, power inverter, radial distribution grid and protection devices.

2.1. PHOTOVOLTAIC POWER PLANT

The basic element of a PV system is the photovoltaic cell. Cells are grouped to form modules, and these modules can be grouped to form photovoltaic arrays. The term array is usually understood as a numerous PV cells connected in series and/or parallel. In Figure 1 equivalent circuit model of a PV array is presented.

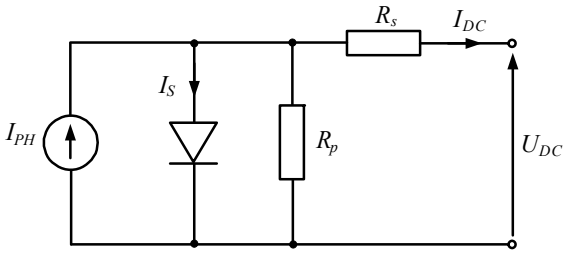

Fig. 1. Equivalent circuit of a PV array

This model consists of an ideal current source, a diode and shunt resistor connected in parallel with the current source and a series resistor.

The output terminal current of modelled photovoltaic array I_{DC} and thereby the I–V characteristic of a practical array may be described by the following equation [6, 7, 12]:

$$I_{DC} = N_p \cdot I_{PH} - N_p \cdot I_S \left(e^{\left(\frac{U_{DC} + R_s \cdot I_{DC}}{a \cdot N_s \cdot V_T} \right)} - 1 \right) - \frac{U_{DC} + R_s \cdot I_{DC}}{R_p} \tag{1}$$

where: N_p is a number of solar modules arranged in parallel, I_{PH} is a photocurrent (light-generated current), I_s is a cell saturation current, R_s is a series resistance, a is an ideal factor (diode constant), N_S is a number of solar modules arranged in series, V_T is thermal voltage, R_p is a shunt resistance.

Photovoltaic current is calculated according to following equation [6, 7, 12]:

$$I_{PH} = (I_{SC} + K_I \cdot (T_C - T_{ref})) \cdot \lambda \tag{1}$$

where: I_{SC} is a short-circuit current, K_I is a short-circuit current temperature coefficient, T_C is cell's working temperature, T_{ref} is a nominal cell's working temperature, $\lambda = G/G_n$ is an insolation level, G is a working irradiation and G_n is a nominal irradiation.

The cell saturation current, in turn, is given as [6,7,12]:

$$I_S = (I_{SC} + K_I \cdot (T_C - T_{ref})) \cdot \left(e^{\left(\frac{V_{OC} + K_V (T_C - T_{ref})}{a \cdot V_T} \right)} - 1 \right)^{-1} \tag{1}$$

where: V_{OC} is a cell open-circuit voltage, K_V is a open-circuit voltage temperature coefficient.

It has been assumed that main parameters of a single PV module are [7]:

$$P_m = 53 \text{ W}; I_{SC} = 3.35 \text{ A}; V_{OC} = 21.7 \text{ V}; V_m = 17.4 \text{ V}; I_{m.} = 3.05 \text{ A}$$

Therefore, 50 MW plant requires 943400 pieces of such PV modules. To simplify the PV model, all modules were arranged in one array. Such model offers a good compromise between simplicity and accuracy. To confirm accuracy of the model, *I-V* and *P-V* characteristics under various operating conditions are presented. In Figure 2 both *P-V* and *I-V* characteristics of modelled array under nominal insolation and cells temperature are shown, whereas Fig. 3 presents *P-V* characteristics of power plant operating under various irradiance and cells temperature.

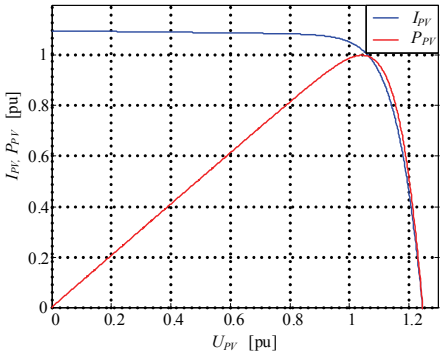

Fig. 2. I-V and P-V characteristics of modelled PV array for nominal insolation and modules temperature

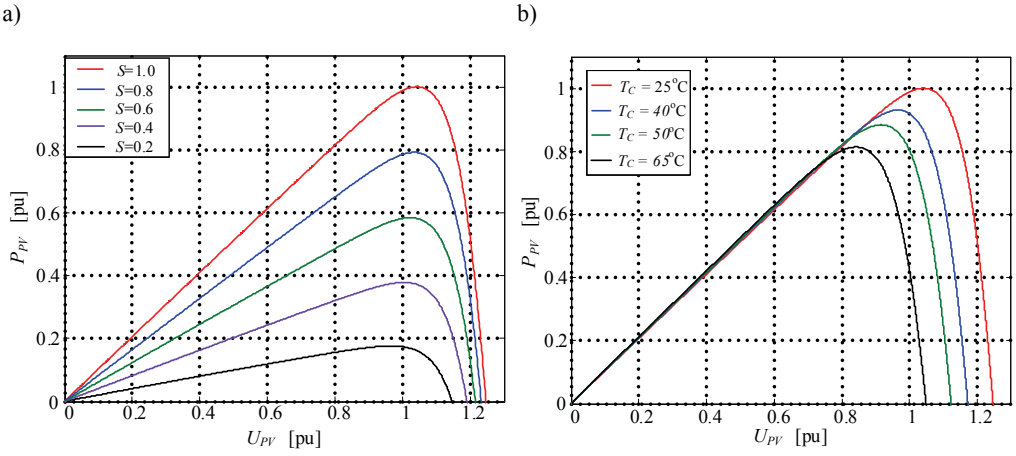

Fig. 3. P-V operation characteristics of modelled PV plant at: a) different insolation conditions; b) different cells temperature conditions

It can be seen that behaviour of the modelled PV power plant showed close approximation of the model characteristics to the real characteristics based on experimental data which are presented in other papers [6, 7, 12].

The complete photovoltaic generation system consists of: a PV array, a full bridge switching converter, AC filter, active and reactive power controllers, Pulse Width Modulation (PWM) module and step-up transformer, as depicted in Fig. 4.

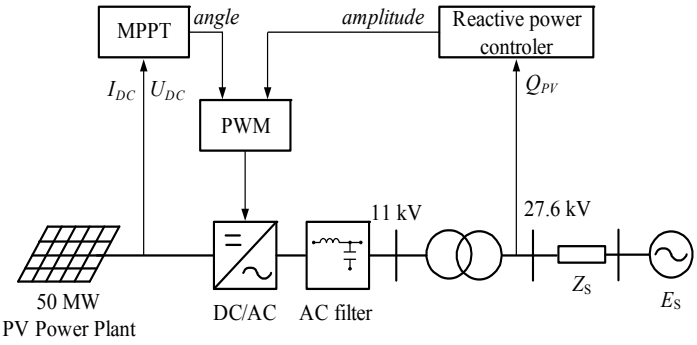

Fig. 4. I P-V operation characteristics of modelled PV plant at different cells temperature conditions

The grid-connected 6-pulse IGBT inverter converts the DC into AC voltage, at frequency equal to the nominal utility grid one. To generate firing signals of the inverter, PWM method was employed. The PWM module was governed by two controllers. The first was responsible for appropriate reactive power generation (it was assumed that reactive power generated by PV power plant should by equal to zero). To generate maximum real power available under actual operating conditions (temperature and irradiance), PWM module was controlled by MPPT block. For tracking the maximum power point (MPPT) of the PV power plant, current (IDC) and the dc-link voltage (UDC) are monitored. Incremental conductance (IncCond) method was used to realize MPPT [3,6]. Additionally, maximal current converted by inverter was limited to 1.5–2.0 times rated current of the PV power plant. To achieve appropriate quality of generated energy (reduce THD factor), LC low-pass harmonic filter was employed.

Such photovoltaic power generation model approximates dynamic response of a large number of channels (sets of PV array, inverter and low voltage transformer) at a point of common coupling [7,12]. To study operating performance of prepared model, two disturbances scenario was simulated.

In Figure 5, plots of PV power change observed behind the step-up transformer under sudden changes of insolation are presented. First the irradiance decreased from 1000 W/m^2 to 600 W/m^2 at 0.7 s and then went back up to the initial value at 1.2 s. A stable operation of the PV system can be observed.

The grid-connected PV power plant responded promptly to sudden change of ambient conditions without any significant overshoot.

In Figure 6, PV power plant phase currents under a persistent three-phase fault at the step-up transformer busbar are presented. It may be observed that right after fault inception short-circuit current form PV plant was limited to the preset value (1.6 times the rated current in this case). If the pickup current of the overcurrent protection is set above this level, PV plant will supply this fault until undervoltage protection operate. In the presented case, fault was cleared after about 0.3 s from the beginning of disturbance.

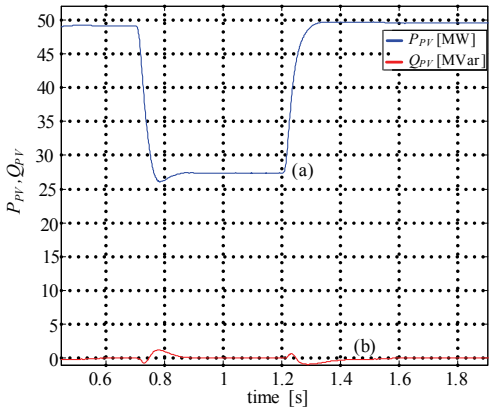

Fig. 5. PV power plant response during sudden change of insolation: a) active power; b) reactive power

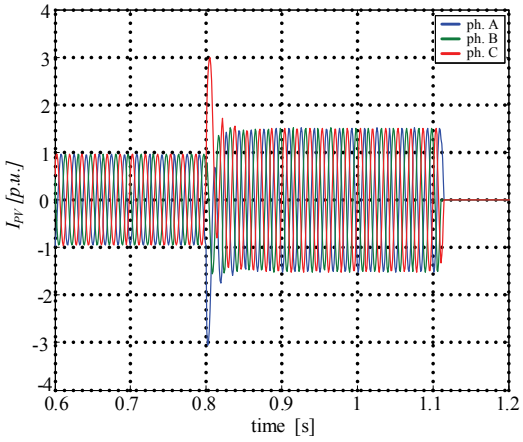

Fig. 6. PV power plant current under long-lasting three-phase fault at the PV station busbar

2.2. TEST DISTRIBUTION NETWORK

Single line diagram of full modelled MV network is presented in Fig. 7. It contains a 50 MW PV power plant – described earlier – connected to a 27.6 kV distribution

feeder. The distribution feeder is supplied by a substation of 70 MVA transformer. Power is transmitted to customers through both cable and overhead lines of lengths varying between 0.5 km and 5.0 km. In the investigations, various impedances of system E_s were considered, to analyse three cases of varying level of PV penetration (i.e., 10%, 30% and 45%).

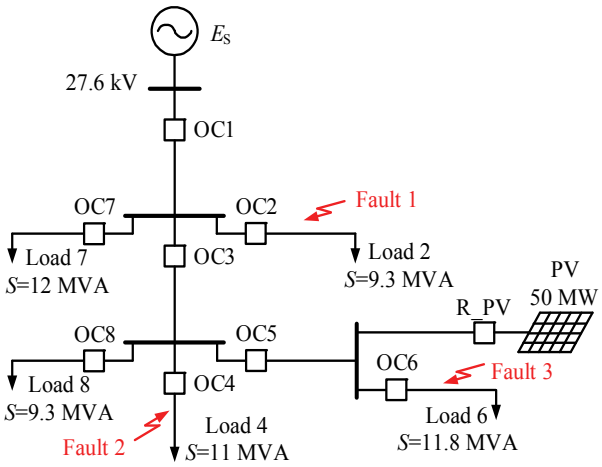

Fig. 7. Schematic diagram of distribution network with PV generation system used in the PSCAD

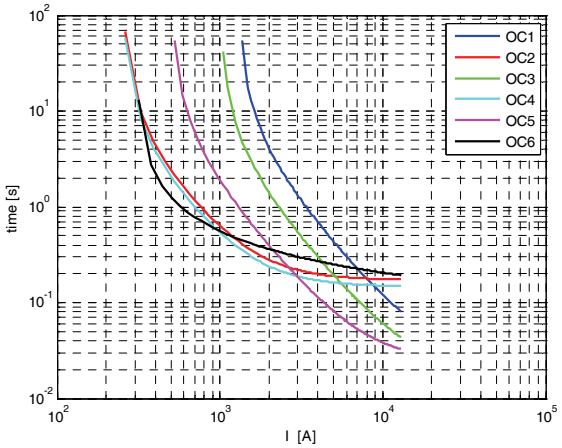

Fig. 8. Time-current curves of overcurrent relays in the distribution system

The model was used for studying three fault scenarios: F_1, F_2 and F_3, as shown in Fig. 7. Overcurrent relays OC1–OC6 were set to operate as fast as possible for faults in the primary zone, and with appropriate delay for faults in the backup zones. Moreo-

ver, the settings must be below the minimum fault current for which they should operate, but not operate on all normal and other load conditions. All relays were set according to these requirements and properly coordinated for system without PV power plant. Figure 8 shows the time-current characteristics of the relays.

3. TEST RESULTS

In this section, the fault contribution of PV grid-connected generation was surveyed. To make results more realistic, various operating conditions of PV arrays have been taken into account such as, operating cells temperature that affects PV characteristics shape as well as insolation that has essential effect upon the maximum of PV power. Since the basic aim of the research was to analyse influence of the PV system on distribution system protection performance (i.e., overcurrent protection), these simulations were done with and without photovoltaic power generation. A large number of fault scenarios have been simulated and relay performance has been investigated. The results for system with and without PV power generation were then compared to assess the performance of the distribution system protection. In this paper, only two cases are shown because of space limitations.

Case 1 is for a three-phase fault at point Fault1. The level of the PV penetration was equal to 30% and overcurrent protection settings remained unchanged as for the system without PV power plant. Figure 9 shows that even if the inverter would continue to feed the fault, it would be at a level below 2 times rated current of the unit. Obviously, this current affects the short-circuit current, as observed when Fig. 10a and Fig. 10b are compared.

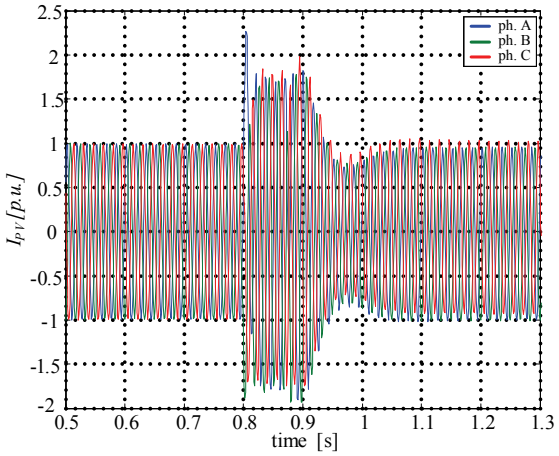

Fig. 9. PV power plant current for Case 1

As far as protection performance is concerned, it has been noticed that even if overcurrent relays settings had not been changed, protection relays were still well coordinated and no maloperations were observed. As shown in Fig. 11, relay OC2 properly cleared the fault. Obviously, tripping time is shorter when fault is fed both from the utility and from PV power plant. Basically, in most of the investigated cases, connection of the PV power plant to the grid did not require any changes of OC relay settings.

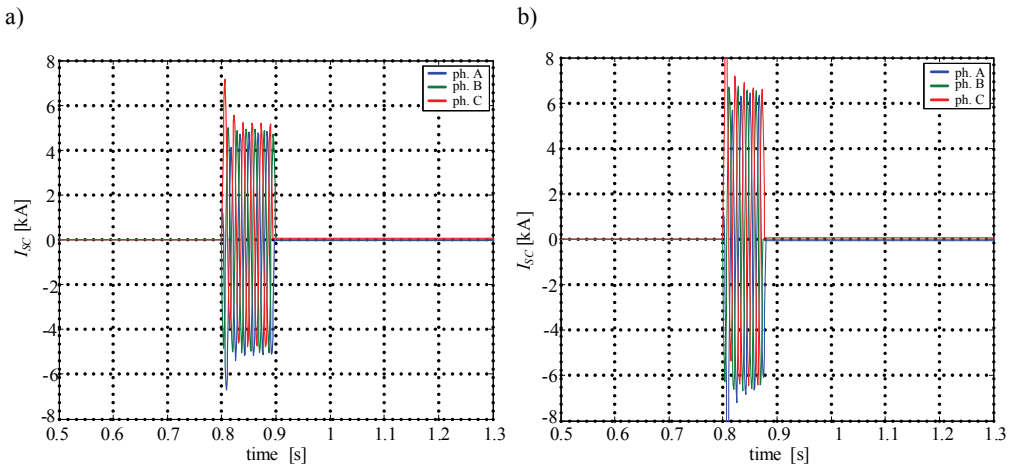

Fig. 10. Short-circuit currents for Case 1: a) without PV power plant; b) with PV power plant

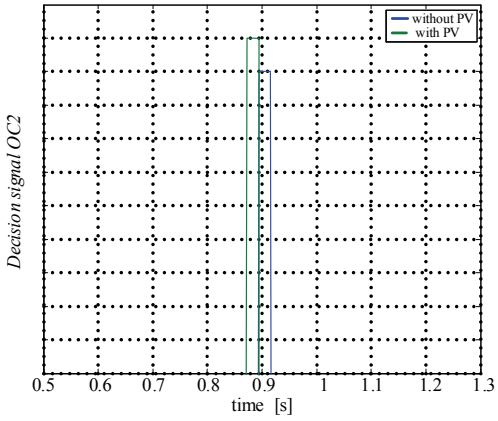

Fig. 11. Decision signals of overcurrent protection OC2 for Case 1

Case 2 is a three-phase fault at point Fault3. The level of the PV penetration was equal to 45% and overcurrent protection settings again remain the same as for the system without PV power plant. In Figure 12, short-circuit current contribution from

grid-connected PV power plant is shown. Although PV current is once again less than twice the inverter's rated output current as seen in Fig. 13, but the contribution is relatively higher as compared to Case 1. But, there is no unselective tripping. The fault was cleared by the relay OC6, as shown in Fig. 14. However, because of this clearance, PV power plant started transferring all generated power through OC5. Since OC5 was not set for such scenario, it can be observed that after few seconds a trip signal is issued, as shown in Fig. 15. This kind of situation should be taken into account. To prevent undesirable tripping in the mentioned case, OC5 should be set properly or a directional time-overcurrent relay may be applied.

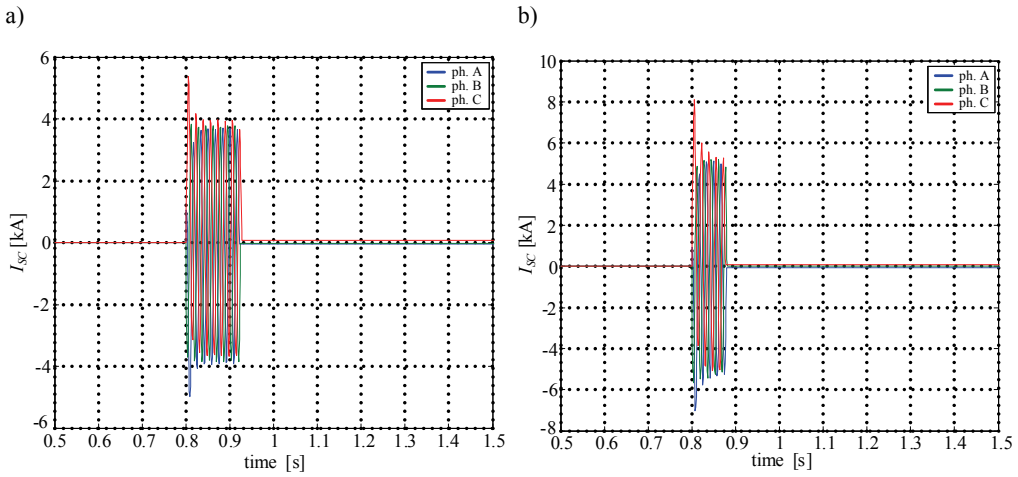

Fig. 12. Short-circuit currents for Case 2: a) without PV power plant; b) with PV power plant

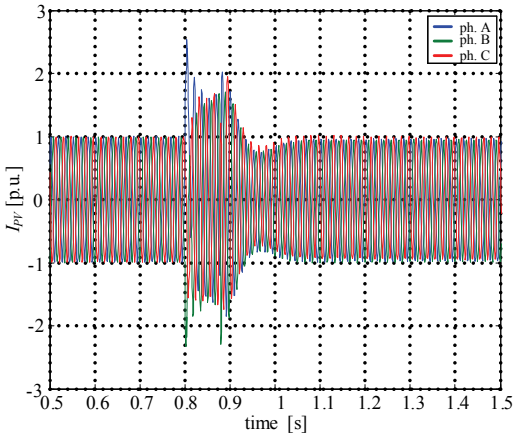

Fig. 13. PV power plant current for Case 2

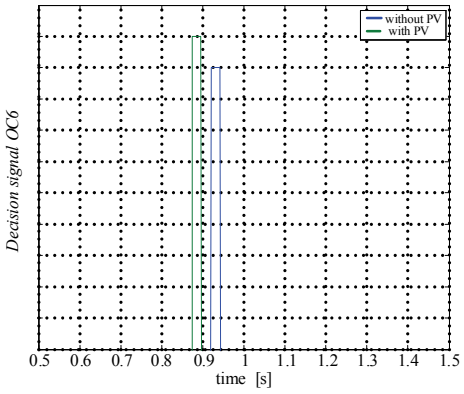

Fig. 14. Short-circuit currents for Case 2: a) without PV power plant; b) with PV power plant

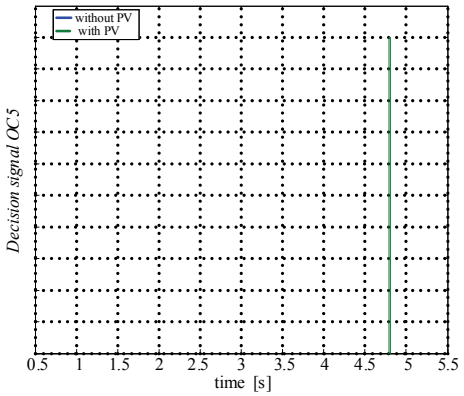

Fig. 15. Short-circuit currents for Case 2: a) without PV power plant; b) with PV power plant

4. CONCLUSION

In the paper, the fault contribution of the grid-connected photovoltaic power plant is discussed. The dynamic model of a PV power plant interconnected to radial distribution network is presented. Using this model, it was possible to investigate issue at hand.

Large number of simulation cases confirmed that even for large scale PV power plant fault contribution is insignificant. Due to limitation of maximum power inverter current, it can be assumed that total fault contribution from PV power plant does not exceed twice the PV power plant rated current. Additionally, when PV system is properly protected (i.e. overcurrent, overvoltage and anti-islanding protections) its fault contribution is also limited in time. For these reasons, there should not be any problem with relays coordination when large scale PV power plant is connected to the grid. Un-

doubtedly utility service should be careful when the level of the PV power plant penetration is high. Then, a dedicated study is recommended and sometimes coordination with directional units may be required.

Although impact of grid-connected PV power plant on the protection performance is not significant, it must be noted that short-circuit current levels will increase. This must be taken into consideration when short-circuit capacity requirements of power system devices (e.g. circuit breakers) are analysed.

REFERENCES

[1] BAGHZOUZ Y., *Voltage Regulation and Overcurrent Protection Issues in Distribution Feeders with Distributed Generation – A Case Study*, Proceedings of the 38th Annual Hawaii International Conference on System Sciences (HICSS '05) – Track 2, Big Island, Hawaii, January 03–06, 2005.

[2] CRUZ J., GOMEZ P., *Real Problems in Utility High Voltage Network due to Grid Connected Photovoltaic Power Generation. The experience of Endesa*, International Conference on Renewable Energies and Power Quality (ICREPQ '10), Granada (Spain), 23–25 March 2010.

[3] ESRAM T., CHAPMAN P.L., *Comparison of Photovoltaic Array Maximum Power Point Tracking Techniques*, IEEE Transactions on Energy Conversion, Vol. 22, No. 2, June 2007, pp. 439–449.

[4] GEIDL M., *Protection of Power Systems with Distributed Generation: State of the Art*, Power Systems Laboratory Swiss Federal Institute of Technology (ETH) Zurich, 20 July 2005.

[5] HUANG T, WANG B., JIANG B., DONG X., BO Z., *A novel control scheme of photovoltaic power plant in islanding operation*, Challenges and Opportunities of the Electric Power Industry in an Uncertain Era, CEPSI 2010, Taipei, Taiwan, October 24–28, 2010, paper ID PP0201002.

[6] KIM S., JEON J.,CHO C., KIM E., AHN J., *Modeling and simulation of a grid-connected PV generation system for electromagnetic transient analysis*, Elsevier, Solar Energy, 83, 2009, pp. 664–678, 21 November 2008.

[7] NEMA R.K., NEMA S., AGNIHOTRI G., *Computer Simulation Based Study of Photovoltaic Cells/Modules and their Experimental Verification*, International Journal of Recent Trends in Engineering, Academy Publisher, Vol. 1, No. 3, May 2009, pp. 151–156.

[8] RUANGROTISN N., CHENVIDHYA D., KIRTIKARA K., WATTANAVICHEAN K., MUENPINIJ B., SANGSWANG A., *A Power Quality Study of a PV Grid-Connected System Due to Load Conditions*, Proc. 17th International Photovoltaic Science and Engineering Conference (PVSEC17), December 2007, Fukuoka, Japan.

[9] SHAHNIA F., HOSSEINI S., *Power Quality Improvement of PV Power Generation Systems Using Hybrid Filter*, Jordanian International Electrical & Electronics Engineering Conference 2006, March 14–16, 2006, Amman, Jordan, paper ID 223.

[10] TAN Y.T., KIRSCHEN D.S., JENKINS N., *Impact of a Large Penetration of Photovoltaic Generation on the PowerSystem*, CIRED 17th International Conference on Electricity Distribution Barcelona, 12–15 May 2003.

[11] TURCOTTE D., KATIREAI F., *Fault Contribution of Grid-Connected Inverters*, IEEE Electrical Power and Energy Conference, October 22–23, 2009, Montreal, Quebec, Canada, pp. 1–5.

[12] VILLALVA M.G., GAZOLI J.R., FILHO E.R., *Modeling and Circuit-Based Simulation of Photovoltaic Arrays*, 10th Brazilian Power Electronics Conference (COBEP), 2009.